Dharmapandit et al. Protection and Control of Modern Power Systems (2017) 2:30
DOI 10.1186/s41601-017-0062-0

Protection and Control of Modern Power Systems

ORIGINAL RESEARCH Open Access

A fast time-frequency response based differential spectral energy protection of AC microgrids including fault location

O. Dharmapandit[1], R. K. Patnaik[2] and P. K. Dash[1*]

Abstract

This paper proposes a pattern recognition based differential spectral energy protection scheme for ac microgrids using a Fourier kernel based fast sparse time-frequency representation (*SST* or simply the sparse S-Transform). The average and differential current components are passed through a change detection filter, which senses the instant of fault inception and registers a change detection point (*CDP*). Subsequently, if *CDP* is registered for one or more phases, then half cycle data samples of the average and differential currents on either side of the *CDP* are passed through the proposed *SST* technique, which generates their respective spectral energies and a simple comparison between them detects the occurrence and type of the fault. The *SST* technique is also used to provide voltage and current phasors and the frequency during faults which is further utilized to estimate the fault location. The proposed technique as compared to conventional differential current protection scheme is quicker in fault detection and classification, which is least effected from bias setting, has a faster relay trip response (less than one cycle from fault incipient) and a better accuracy in fault location. The significance and accuracy of the proposed scheme have been verified extensively for faults in a standard microgrid system, subjected to a large number of operating conditions and the outputs vindicate it to be a potential candidate for real time applications.

Keywords: Microgrid, Differential spectral energy protection, Time-frequency representation, Fault classification, Fault location

1 Introduction

To take care of a number of issues, such as rise in energy demand; depletion of conventional energy resources (such as coal and fossil fuels); pollution and hazards; etc., the use of the distributed energy resources (*DER*), such as wind, solar, fuel cells etc., has been demonstrated as a feasible solution. According to *IEEE* standard 1547.4, networks constituting one or more *DER*, energy storage devices (*ESD*) and loads are termed as microgrids, which must have the capability and reliability to operate, both in the grid connected mode (*GCM*) as well as islanded modes (*IM*), respectively [1]. Improvement of power quality, consistency, energizing the islanded region during utility outage (which may be intentional enabling the maintenance of the utility), compensating the peak power demands, etc., are the key benefits of the microgrids [2]. Though the widespread implementation of these low voltage microgrids, and their interconnection with the existing utilities are very much beneficial, some of their issues such as control of voltage and frequency, stability, protection of the *DER*, etc., are very much significant to be investigated [3, 4]. In this regard, protection of the distribution lines present in the local microgrid network is an important and challenging issue, which has been addressed in this paper.

In the *GCM*, the fault current (*FC*) is contributed by the *DER* and the utility, where as in the *IM*, the *FC* is contributed mostly by the *DER* and partly by the *ESD*. Thus the *FC* during *IM* is subsequently small in magnitude as compared to the *GCM*. The distribution line protection mechanism must enable the safe and reliable operation of the microgrid subjected to faults, both in the *GCM* and *IM*, respectively [5]. Over current relays

* Correspondence: pkdash.india@gmail.com
[1]Electrical Engineering Department, Institute of Technical Education and Research, Institute of Technical Education and Research, Siksha O Anusandhan University, Bhubaneswar -751030, India
Full list of author information is available at the end of the article

[6–8], are attractive for *GCM* of the microgrids, but due to the intermittent nature of the power generation by the *DER*'s, the bandwidth of the *FC* becomes very wide, which makes them unreliable. In this regard, some communication based protection strategies [9, 10], and adaptive relay setting based protection strategies [11, 12] have been proposed for microgrids. These strategies are much effective in *GCM* of operation of the microgrid, but the response for the *IM* of operation of the microgrid has not been investigated. Some of the other techniques such as sequence component based methods [13] are very much complex, as the synchronization of the relay depends on manifold settings on the plagiaristic sequence components. In this regard, over current differential protection scheme [14] has been proposed for the microgrid which are effective in the *GCM* but are unreliable in *IM* due to limited over current magnitudes in the post fault region. Besides the intermittent power generations of the *DER* in *IM* require adaptive setting of the over current relays. A current differential relay based microgrid protection scheme [15] has been investigated, but it requires proper CT settings to distinguish between internal and external faults.

A digital relays based communication system [16] independent of time-synchronization of measured currents has been proposed for the differential current protection of microgrids. One of the basic disadvantages of such method was its concentrated performance in issuing relay trip signal as time synchronization is a key pointer. In this regard, and as an effective solution to the above mentioned issue, a microgrid protection strategy based on differential energy [17], was proposed. This strategy endows a reduced amount of sensitivity towards the synchronization error, as compared to the differential current signals, which are difference of information in time. In this method, initially the current signals measured on the either side of the distribution line are through the S-transform, which computes the respective energy at each end. These are subsequently subtracted to evaluate the differential energy component. This method is effective in protection of microgrids, both in *GCM* and *IM* operations. In spite of this, the method has a number of shortcomings. Firstly, as energy of a signal is a function of its square, and as the differential energy in that proposed method is a function (difference) of the absolute of the square of the current signals, thus an optimized bias setting (depending on the widespread operating conditions) is highly required. Secondly, the investigations were based on S-transform, which has a higher computational overhead of the order of $O(N^2 \log N)$. Thirdly, as a large number of test samples need to be passed through the S-transform, hence the computational complexity of the algorithm is very high, which is significantly reflected by the relay trip time which is greater than approximately three cycles. Finally, the paper did not investigate the fault location aspect, which is significantly important from the protection point of view for the distribution line protection in microgrids. Taking into account the above discussions, there is a strong motivation for the development of a fast and reliable protection scheme for the distribution line, which must be faster in fault detection and classification, accurate in fault location and issue a quick relay trip signal both in the *GCM* and *IM* operations of the microgrid subjected to different levels of the *DER* penetrations, respectively.

This paper proposes a differential spectral energy scheme (*DSE*) for distribution line protection in a microgrid using a sparse Fourier kernel based fast time-frequency representation (*SST*). A matrix version of this scheme has been presented in reference [18] using intelligent frequency scaling methods which is almost 30 times faster than the proposed generalized S-Transform outlined in [17]. The method presented in this paper is immune to *CT* saturation as it generates a tripping time less than half cycle of the 50 or 60 Hz waveform. In order to ensure a differential protection scheme, the current (in each phase) at both ends of a distribution line are initially measured and processed so as to derive the respective average and differential components. Further, these components are passed through a change detection filter technique, whose output registers the occurrence of fault as well as the change detection point (*CDP*) depending upon a fault criterion. Subsequently, if *CDP* is registered for a particular phase, then half cycle data samples of the average and differential currents on either side of the *CDP* are passed through the proposed *SST* technique, which generates the differential current spectral energy (*DSE*) and the average current spectral energy (*ASE*). The occurrence of fault is verified if the maximum of *DSE* in the post fault region is higher than the *ASE* plus some bias (which is required to avoid misdetection and is tuned manually), and this ignites the fault location algorithm, based on the proposed *SST* technique. The proposed *DSE* technique as compared to conventional discrete Fourier transform (*DFT*) and differential current protection scheme has a number of advantages, such as reduced computational complexity, reduced effect of bias setting for fault detection, quicker fault detection and classification and faster relay response time as well as better accuracy of fault location. The significance and accuracy of the proposed scheme has been verified extensively for a distributed generation (DFIG wind farm) based standard microgrid [19], subject to a large number of different operating conditions such as mode of operation of the microgrid (grid connected or islanded), type of fault ((single line to ground faults (*L*-g), double line to ground faults (*LL*-g), and triple line

to ground fault (*LLL*-g), fault resistance, fault distance ratio, and the level of penetration of the DG, respectively, in the MATLAB/ Simulink environment. Finally the outputs as shown in the simulation and result section reveal that the proposed *SST* based *DSE* for the distribution line protection, is a robust and reliable mechanism, which is effective for both the grid connected and islanded mode of operation of the microgrid subject to various level of *DG* penetrations, respectively, and endowed with a fast detection time (less than half cycle), is vindicated as a potential candidate for the real time applications.

2 Methods

2.1 Time-frequency response (*TFR*) analysis

The linear Time-frequency (*TF*) analysis algorithm like S-Transform (*ST*) and its variants have been applied to analyse power quality disturbances earlier. *TFR* is a reflection of time evolving concentration of various frequency components present in a signal, giving rise to unique signatures for each class of signal undergoing changes due to a disturbance or fault. Specifically, the *ST* has gained special attention due to its Fourier kernel and absolute phase reference. The standard expression of a linear *TF* transform is:

$$S(\tau,f) = \int_{-\infty}^{\infty} x(t)\omega(\tau-t,f)\exp(-i2\pi ft)dt \tag{1}$$

where $x(t)$is the signal to be analysed and $\omega(\tau,f)$is an adjustable Gaussian window, τ and t are time variables, f is the signal frequency. A generalized window function [] is used here to provide a better control of the time and frequency resolutions by varying the shape and property of the window.

Thus

$$\omega(\tau-t,f) = \frac{1}{\sigma(f)\sqrt{2\pi}}\exp\left(\left(-(\tau-t)^2/2\sigma^2(f)\right)\right) \tag{2}$$

and the standard deviation of the window function $\sigma(f)$ is given by

$$\sigma(f) = \frac{\alpha}{a+b|f|^c} \tag{3}$$

where α, and b are scaling parameters that control the number of oscillations in the window (frequency resolution); a and c are positive constants. The window broadens in the time domain with the increase of α which results in an increase of frequency resolution in the frequency domain. The value of c lies between 0 and 1 for effective catching of damped hidden frequencies. The discrete version of the *ST* is obtained for set of signal samples $x(k)$, $k = 1, 2, \ldots \ldots \ldots, N$ as

$$S(j,n) = \sum_{k=1}^{N} X[k+n] \times \exp\left\{\frac{-2\pi^2k^2\alpha^2}{(a+bm^c)^2} + \frac{i2\pi kj}{n}\right\}, n\neq 0 \tag{4}$$

and

$$X(n) = \sum_{k=0}^{N-1} x(k)\exp\left(\frac{-2\pi ink}{N}\right) \tag{5}$$

where $x\ [k + n]$ is the shifted *DFT* of the signal samples $x(k)$ by n, and the frequency index $m = n/NT_s$; T_s is the sampling time interval, $j = 1,2,\ldots\ldots,N$, *and* $n = 1,2,\ldots\ldots\ldots,N$.

Although the *ST* has gained special attention due to its Fourier kernel and absolute phase reference, its reference to Fourier basis in *ST* enables direct interpretation of spectral component variation standards, and this property is the prime advantage of *ST* from the perspective of measurement of parameters and estimation, and pattern recognition. Although the conventional S-transform technique can be used for signal estimation purposes, but it is computationally complex and takes long time for estimation and therefore is not suitable for real-time applications. A faster version of discrete *S*-Transform has been proposed recently in reference [11] by one of the authors, which is made sparse with complex sinusoid modulated Gaussian atom and new frequency scaling, and band pass filtering techniques. The Sparse S-Transform (*SST*) results in drastic reduction of computational complexity with accurate *TFR*. The *SST* is evaluated only at the significant frequencies, which satisfy set cut-off amplitude obtained from the *DFT* of the signal. Rest of the frequencies with lower amplitudes need not be processed for practical purposes. The following steps are used to formulate the sparse *SST* in a matrix form:

Step 1: DFT of the time-domain signal samples $x(k)$, $k = 1, 2, \ldots \ldots \ldots, N$yield the following row vector:

$$B = [b_1, \ldots b_n, \ldots\ldots b_N]$$

where

$$b_n = \sum_{k=1}^{N} a_k \exp\left(\frac{-2\pi i(n-1)(k-1)}{N}\right) \tag{6}$$

Step 2: The window B of N frequencies is rotated and concatenated to obtain the data matrix D as

$$D_{M\times N}=\begin{bmatrix} b_2 & b_3 & \dots & b_N & b_1 \\ b_3 & b_4 & \dots & b_1 & b_2 \\ \dots & \dots & \dots & \dots & \dots \\ b_M & b_{M+1} & \dots & b_{M-2} & b_{M-1} \\ b_{M+1} & b_{M+2} & \dots & b_{M-1} & b_M \end{bmatrix} \tag{7}$$

where each of its elements is given by

$$D_{(m,n)}=\begin{Bmatrix} b_N & if((m+n)=N) \\ b_{(m+n)\bmod N} & otherwise \end{Bmatrix} \tag{8}$$

and the frequency index $m = 1, 2,\dots\dots\dots, M$, and the time index $n = 1,2,\dots\dots\dots,N$. Further according to Nyquist theorem $M = N/2$.

Step 3: For each set of N signal samples, a two dimensional Gaussian window matrix in both time and frequency domain is formed whose elements are obtained as

$$C(m,n)=\exp\left(\frac{-2\pi^2\alpha^2(n-1)^2m}{(a+bm^c)^2}\right)+\exp\left(\frac{-2\pi^2\alpha^2(N-n+1)^2m}{(a+bm^c)^2}\right) \tag{9}$$

Step 4: A harmonic scaling matrix $G(m,n)$based on an intelligent selection of dominant frequency components present in the signal is then formulated. This, however, depends on frequency partitioning and filtering. In power systems, the frequencies which are the integral multiple of the fundamental frequency are of major interest. So in the formulation of the *SST* the scaled frequencies are chosen from the fundamental and harmonic frequency components instead of evaluating at all the frequencies. Thus the *G (m, n)* matrix is obtained as

If h = odd number,

$$G(m,n)=1, m\in(f,3f,5f,\dots.hf), Otherwise\ G(m,n)=0. \tag{10}$$

Step 5: Multiply the data matrix D (m, n) with the Scaling Matrix *G (m, n)* element-by-element wise to obtain

$$GG=D_{M\times N}\ \mathbf{o}\ G_{M\times N} \tag{11}$$

Where **o** denotes the Hadamard product [20] (element-by element multiplication) of the matrices.

Step 6: The window matrix C obtained in step 3 is multiplied with the GG matrix element-by element wise to acquire the windowed frequency domain information to obtain

$$H=GG_{M\times N}\ \mathbf{o}\ C_{M\times N}$$

where

$$H_{M\times N}=\begin{bmatrix} h(1,1) & \dots & h(1,n) & \dots & h(1,N) \\ \dots & \dots & \dots & \dots & \dots \\ h(m,1) & \dots & h(m,n) & \dots & h(m,N) \\ \dots & \dots & \dots & \dots & \dots \\ h(M,1) & \dots & h(M,n) & \dots & h(M,N) \end{bmatrix} \tag{12}$$

Step 7: Apply one-dimensional inverse Fourier transform along each row of *H (m, n)* to obtain the *SST* as

$$SST(m,n)=\frac{2}{N}\sum_{k=0}^{N-1}H(m,k)\exp(i2\pi nk/N) \tag{13}$$

and replacing the frequency index m by actual signal frequencies and time index n by time, *SST* is obtained as

$$SST_{M\times N}=\begin{bmatrix} s(f_1,t_1) & \dots & s(f_1,t_n) & \dots & s(f_1,t_N) \\ \dots & \dots & \dots & \dots & \dots \\ s(f_m,t_1) & \dots & s(f_m,t_n) & \dots & s(f_m,t_N) \\ \dots & \dots & \dots & \dots & \dots \\ s(f_M,t_1) & \dots & s(f_M,t_n) & \dots & s(f_M,t_N) \end{bmatrix} \tag{14}$$

The important issue is proper selection of generalized Gaussian window parameters. Authors have proposed a technique for enhancing *TFR* energy distribution according to a performance measure (*PM*) at any frequency index k. The optimization of this *PM* reassigns energy concentration of the *TFR*.

$$PM_{[\alpha,a,b,c]}(n)=\sum_{n=0}^{N}\left(\frac{1}{SST_{[\alpha,a,b,c]}(m,n)}\right)^{0.25} \tag{15}$$

At each frequency index *m*:

$$[\alpha,a,b,c]_{optimized}=\arg\left(\max[PM(n)]\right) \tag{16}$$

To obtain the maximum value of the performance measure *PM* the shape of the window is varied for each analysis frequency to obtain an accurate time-frequency distribution of the energy concentration. From Eq. (12) the optimization is performed by integrating *SST* over the frequency domain that preserves the frequency marginal of the transform without the loss of information regarding amplitudes of the spectral components. For a sinusoidal signal with normalized amplitude of 1.0 per unit, the optimization yields the values of $a = 0$, $b = 1.0$, $c = 1.0$, and$\alpha = 0.9$.

The output of the *SST* algorithm is a complex matrix, which is sparse because of the *FFT*-based frequency selection. The *M* rows correspond to the *M* frequency points and the *N* columns correspond to the *N* time points. At each time point and frequency point, the signal of that particular frequency is represented by an instantaneous phasor. The multiplication of the Gaussian window for obtaining time information is done with only a few of the *M* values provided by the *FFT* operation. Rest of the rows in *SST* matrix are assigned zero. The output of the *SST* algorithm is a complex matrix, which is sparse because of the *FFT*-based frequency selection. The *M* rows correspond to the *M* frequency points and the *N* columns correspond to the *N* time points. At each time point and frequency point, the signal of that particular frequency is represented by an instantaneous phasor. To demonstrate the speed of execution of the *SST*, the conventional *ST* takes around 0.0580 s for processing 10 cycles of data (64 samples per cycle), whereas the *SST* algorithm with harmonic scaling consumes significantly less time of 0.005 s. using an Intel Core 2 Duo, 2.4 GHz central processing unit with 4 GB random access memory based signal processor. Thus the speed advantage of the *SST* algorithm is more than 10 times. However, with a smaller cut-off magnitude of the harmonics, the speed can be easily increased to more than 30 times for the automatic scaling based *SST*.

The online *SST* algorithm handles *N* samples at a time for the time-frequency localization of the prominent sinusoids in the actual signal. Effectively, the discretized power signal is segmented into bunches of mutually exclusive sets containing *N* samples. The *SST* operation is therefore represented as:

$$[SST_i]_{M\times N} = SST\left(x_{(i+1)}, x_{(i+2)}, x_{(i+3)} \ldots x_{(i+Ns-1)}, x_{(i+N)}\right) \tag{17}$$

where i = 0, Ns, 2.Ns, 3.Ns…(λ-2).N, (λ-1).N; and λ is a positive integer.

The output of the *SST* algorithm is a complex matrix SST_i which is capable of giving time-frequency localized both instantaneous amplitude and phase information.

The *SST* output is represented as:

$$SST(m,n) = A(m,n)\exp(j\theta j\theta(m,n)) \tag{18}$$

where the amplitude of the SST spectrum =

$$A(m,n) = \sqrt{real([SST(m,n)])^2 + imag([SST(m,n)])^2} \tag{19}$$

at a given frequency m and time index n. The phase angle of the SST spectrum is obtained in a similar way as

$$\theta(m,n) = \arctan\left(\frac{\mathrm{Im}[SST(m,n)]}{\mathrm{Re}[SST(m,n)]}\right) \tag{20}$$

Out of the total M rows in the SST matrix, most of them would have negligible values and hence they are not used for computation. A particular signal is represented by its frequency point or its row in the matrices. In online mode, a phase correction factor is introduced to accommodate the error in phase. The actual phase of a signal with frequency f Hz is given as:

$$\theta_{corrected}(m,n) = \theta(m,n) - 2\pi f/f_s \tag{21}$$

where f_s is the sampling rate in hertz and the phase is represented in radians.

For obtaining the fundamental amplitude and phase angle at the sample number t

$$A_1(t) = \sqrt{(real[s(f_1,t)])^2 + (imag[s(f_1,t)])^2} \tag{22}$$

$$\varphi_1(t) = \tan^{-1}\{(imag[s(f_1,t)])/(real[s(f_1,t)])\} \tag{23}$$

By definition the instantaneous fundamental angular frequency is obtained as

$$f_1 = \frac{d\varphi_1}{dt} = \frac{SH_R \times d(SH_I)/dt - SH_I \times d(SH_R)/dt}{(SH_R)^2 + (SH_I)^2} \tag{24}$$

where

$$\left.\begin{aligned} SH_R &= real[s(f_1,t)] \\ SH_I &= imag[s(f_1,t)] \end{aligned}\right\} \tag{25}$$

The actual phase of a signal with frequency f Hz is given as

$$\theta_{1corrected} = \theta_1(t) - 2(f/f_s)\pi \tag{26}$$

2.2 Differential spectral energy (DSE) for microgrid protection

This section explains the details regarding the proposed fault detection and classification algorithm, whose flowchart is illustrated in Fig. 1.

2.2.1 Differential and average current computation

In a differential protection scheme, the average and differential current components are the two significant

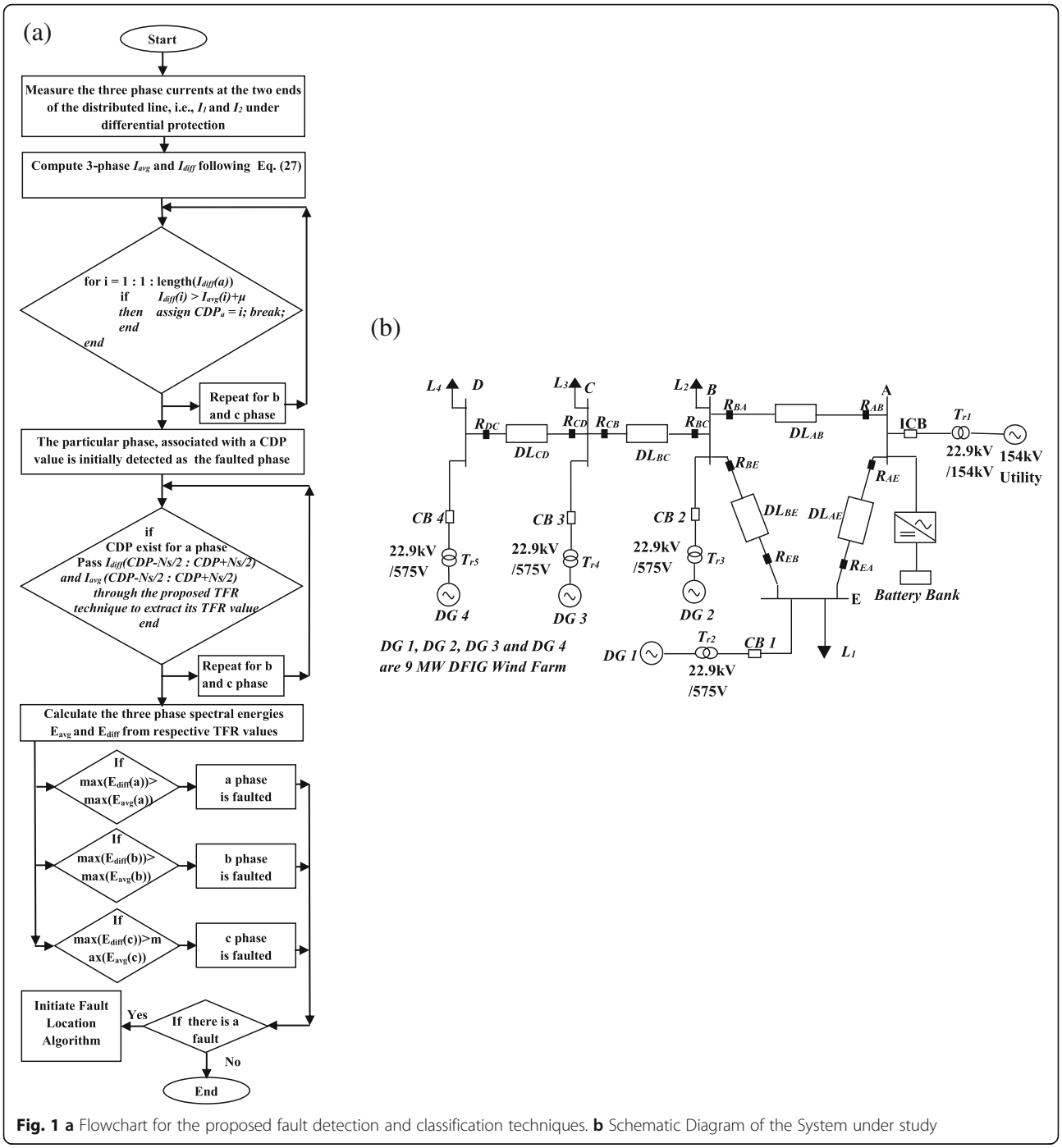

Fig. 1 a Flowchart for the proposed fault detection and classification techniques. **b** Schematic Diagram of the System under study

attributes, which are utilized by the differential relays for their operation and control. In this regard, the three phase instantaneous current samples on either end of the distribution line (under differential protection scheme), i.e., I_1 and I_2 are measured. In this regard, the data from the two ends of the protected zone can be exchanged using a high-speed (<1 ms) and reliable communication channel, where the time synchronization can be achieved by a timing signal obtained from a Global Positioning System transducer, whose delay tolerance is of the order of +/− 3 microsecond [21]. The following computations signifies the instantaneous average current (I_{avg}) and differential current (I_{diff}), respectively:

$$\left.\begin{aligned} I_{avg}(k) &= 0.5 \times (I_1(k) + I_2(k)), \\ I_{diff}(k) &= (I_1(k) - I_2(k)) \end{aligned}\right\} \quad (27)$$

where k is the sampling instant.

2.2.2 Differential proposed change detection filter technique (CDFT) for fault detection

A change detection filter technique (*CDFT*) is utilized to detect any change in the differential current and average current components, respectively. The *CDFT* finds out the cumulative summation of the difference between the reference (previous) cycle and the present cycle to register any alterations in the signal. It is a sample by sample process where the first cycle data is assigned as the reference cycle data, and computation starts from the second cycle.

Suppose N is total number of samples for a signal x (I_{avg} or I_{diff}), which has been sampled with N_s equal to 64 samples per fundamental cycle. Therefore, *CDFT* of the signal x can be mathematically defined as:

$$CDFT_x(i) = CDFT_x(i-1) + \sum_{k=N_s+1}^{N} \{x(k)-x(k-N_s)\} \tag{28}$$

where i is the iteration number, k is the sample number starting from the second cycle, i.e., $N_s + 1$, while the initial $CDFT_x$ i.e., $CDFT_x(0) = 0$.

The corresponding *CDFT* values for the average current and differential current components are assigned as $CDFT_{avg}$ and $CDFT_{diff}$, respectively. It is observed that, under normal operating conditions, $CDFT_{diff}$ should be very low, as nearer to zero, and its value will be less as compared to $CDFT_{avg}$. As soon as there is a fault, it is noted that due to the nature of current flow (bidirectional towards each other), the $CDFT_{diff}$ shoots up very large as compared to $CDFT_{avg}$. The sample number at which the absolute of the $CDFT_{diff}$ crosses the $CDFT_{avg}$ plus some bias (β) is termed as the change detection point (*CDP*) and it registers the first instance of occurrence of the fault. Mathematically, it can be defined as.

For an internal fault, *CDP* is registered whenever:

$$\left|CDFT_{diff}\right| - \left|CDFT_{avg}\right| > \beta \tag{29}$$

For an external fault, *CDP* is not registered as:

$$\left|CDFT_{diff}\right| - \left|CDFT_{avg}\right| < \beta \tag{30}$$

Once *CDP* is registered, it triggers the proposed fault detection technique to extract the time frequency localized spectral energy of the signal. One of the advantage of this method over [17] is that, instead of passing a large number of samples through the proposed time-frequency transform, only one cycle data, i.e., half cycle data for before *CDP* and half cycle data after *CDP* is passed, which considerable reduces the computational burden as well as improves the fault detection timing. Besides the bias ('β ') is difficult to be set and trigger *CDP*, which might give a false impression of the fault occurrence on a given phase. Thus once the change in the average and differential current signals is detected, the signals for each phase will be passed to the proposed *TFR* technique to confirm the occurrence of the fault as well to classify the type of fault.

2.2.3 Differential spectral energy protection based fault classification

After the *CDP* is detected (which is considered as the instant of occurrence of the fault), one half cycles data of the differential and average current samples, both before and after the occurrence of the fault, respectively, are processed by the proposed *SST* technique to obtain the *TFR* as

$$TFR_{avg} = SST(\,[I_{avg}(CDP-Ns/2) \ldots \; I_{avg}(CDP) \ldots \; \ldots\ldots \; I_{avg}(CDP-1+Ns/2)]_{(1\times N_s)}) \tag{31}$$

$$TFR_{diff} = SST(\,[I_{diff}(CDP-Ns/2) \;\; \ldots \;\; I_{diff}(CDP) \;\; \ldots \;\; \ldots\ldots \;\; I_{diff}(CDP-1+Ns/2)]_{(1\times N_s)}) \tag{32}$$

The differential and average spectral energies for each phase are obtained from *TFR*'s as

$$E_{avg} = \left|TFR_{avg}\right|^2, \quad E_{diff} = \left|TFR_{diff}\right|^2 \tag{33}$$

The change in spectral energy at different sampling intervals is found to be quite large and, therefore, the maximum value of both E_{avg} and E_{diff} are considered for fault classification or detection. In this regard, a comparison between the maximum values of differential and average spectral energies is essential to note that the differential energy becomes higher than the average energy during a fault, which is otherwise quite small during normal conditions.

if

$$\max\{E_{diff}(CDP : CDP + (N_s/2))\} \; > \; \max\{E_{avg}(CDP : CDP + (N_s/2))\}$$

then a fault is registered for the particular phase.

The relay tripping point is the sample point at which the spectral energy of the differential current exceeds the spectral energy of the average current plus some bias 'ζ'. Mathematically, relay tripping point is the first instant after fault incipient where $E_{diff} > E_{avg} + \zeta$. This bias setting is only required to avoid any false misdetection and is tuned manually after observing the respective energy values for a large number of simulations.

2.2.4 Proposed TFR based fault classification

The proposed *SST* technique is utilized for locating the approximate distance of occurrence of the fault. For a particular distribution line (under proposed protection scheme), one end is considered as the reference point, and the corresponding instantaneous voltage and current samples at this point are measured. These measured components are passed through the proposed *TFR* technique, which extracts the fundamental amplitude and phase components of the voltage and current samples using Eqs. (21) and (22), respectively. Let the total impedance of the line be X_{L0}. In order to estimate the location of the fault, the apparent impendence, as seen by the relay at the reference point is computed as:

For single phase faults (*L*-g) faults, apparent impedance can be computed as

$$Z_{Apparent} = \frac{V_{phase}\angle\phi_{v,phase}}{I_{phase}\angle\phi_{i,phase} + \left(\left|\frac{Z_0 - Z_1}{Z_1}\right| \times \left(\frac{I_{phase-a}\angle\phi_{ia} + I_{phase-b}\angle\phi_{ib} + I_{phase-c}\angle\phi_{ic}}{3}\right)\right)} \tag{34}$$

where V_{phase}, I_{phase}, $\phi_{v,phase}$ and $\phi_{i,phase}$are the phase values, extracted from the fundamental amplitude and phase angle of the input voltage and current samples, respectively, which are computed from the proposed *TFR* technique. Similarly $I_{phase\text{-}a}$, $I_{phase\text{-}b}$, $I_{phase\text{-}c}$, $\phi_{ia,}$ $\phi_{ib,}$ and ϕ_{ic} are the three phase values, extracted from the fundamental amplitude and phase angle of the input current samples, respectively.

In a similar manner, for double line faults (*LL* and *LL-g*), apparent impedance seen by the relay is computed as:

$$Z_{Apparent} = \frac{V_{line}\angle\phi_{v,line}}{I_{line}\angle\phi_{i,line}} \tag{35}$$

where V_{line}, I_{line}, $\phi_{v,\ line}$ and $\phi_{i,\ line}$ are the line values, extracted from the fundamental amplitude and phase angle of the input voltage and current samples, respectively,

Similarly for triple line faults (*LLL* and *LLL-g*) faults, apparent impedance seen by the relay is computed as:

$$Z_{Apparent} = \frac{V_{phase}\angle\phi_{v,phase}}{I_{phase}\angle\phi_{i,phase}} \tag{36}$$

The resistance, R (in Ω) and reactance, X (in Ω) are calculated from $Z_{Apparent}$ as follows:

$$\left.\begin{aligned} R &= real\left(Z_{Apparent}\right) \\ X &= imag\left(Z_{Apparent}\right) \end{aligned}\right\} \tag{37}$$

For a particular distribution line, we have the prior knowledge of the total reactance of the line (X_{actual}), as well as the total distance of the line (D_{actual}) as well as the actual location of the fault (FL_{actual}). Thus as soon as we calculate the $Z_{Apparent}$, we extract the estimated reactance ($X_{estimated}$) from Eq. (37).

In the next process, we find the estimated *FDR* as:

$$FDR_{estimated} = \frac{X_{estimated}}{X_{actual}} \tag{38}$$

Subsequently, the estimated fault location ($FL_{estimated}$) is derived as:

$$FL_{estimated} = FDR_{estimated} \times D_{actual} \tag{39}$$

Finally, the percentage error in fault location, i.e., *PEFL* (%) is defined as:

$$\text{PEFL}\ (\%) = \frac{FL_{actual} - FL_{estimated}}{FL_{actual}} \times 100\% \tag{40}$$

3 Simulation and results

The single line diagram of the microgrid system [19] under study is as shown in Fig. 2. The five bus (*A*, *B*, *C*, *D* and *E*) distribution system is connected to a 154 kV utility at the point of common coupling, i.e., bus 'A', through a 47 MVA, 22.9 kV/154 kV step-up transformer T_{r1}. The distribution system consists of five distribution feeders (DL_{AB}, DL_{BE}, DL_{AE}, DL_{BC} and DL_{CD}, which are simulated as pi sections [22]), each having two end measurement units through the differential relay pairs, i.e., {R_{AB} and R_{BA}}, {R_{BE} and R_{EB}}, {R_{AE} and R_{EA}}, {R_{BC} and R_{CB}} and {R_{CD} and R_{DC}}, respectively. The distribution system consists of four distributed generation (*DG*) units, (*DG 1*, *DG 2, DG 3* and *DG 4*) each of which is a 9 MW, 575 V, 60 Hz DFIG based wind farm [23], and are connected to the distribution system at buses E, B, C and D through 10.5 MVA, 575v/22.9 kV transformers T_{r2}, T_{r3}, T_{r4} and T_{r5}, respectively. In addition to the *GCM* of operation of the microgrid, an energy storage (battery bank) [20] is installed at the point of common coupling, i.e., bus 'A', so as to formulate a viable microgrid in *IM* of operation. The details regarding the network parameters are specified in the Appendix.

The proposed model is simulated in MATLAB/ Simulink environment with a sampling frequency of 3.84 kHz and fundamental frequency f_0 equal to 60 Hz. Current signals at each end of the feeder under protection are retrieved with the help of relays located at across the respective feeder. Differential current and average current of respective phases are calculated using Eq. (27). *CDFT* of the average current and the differential current are obtained from Eq. (28) using the average and differential current samples, respectively, for the signal. Under healthier operating conditions the *CDFT* of differential current is nearly zero as compared to the *CDFT* of average current. If the *CDFT* of differential current is more

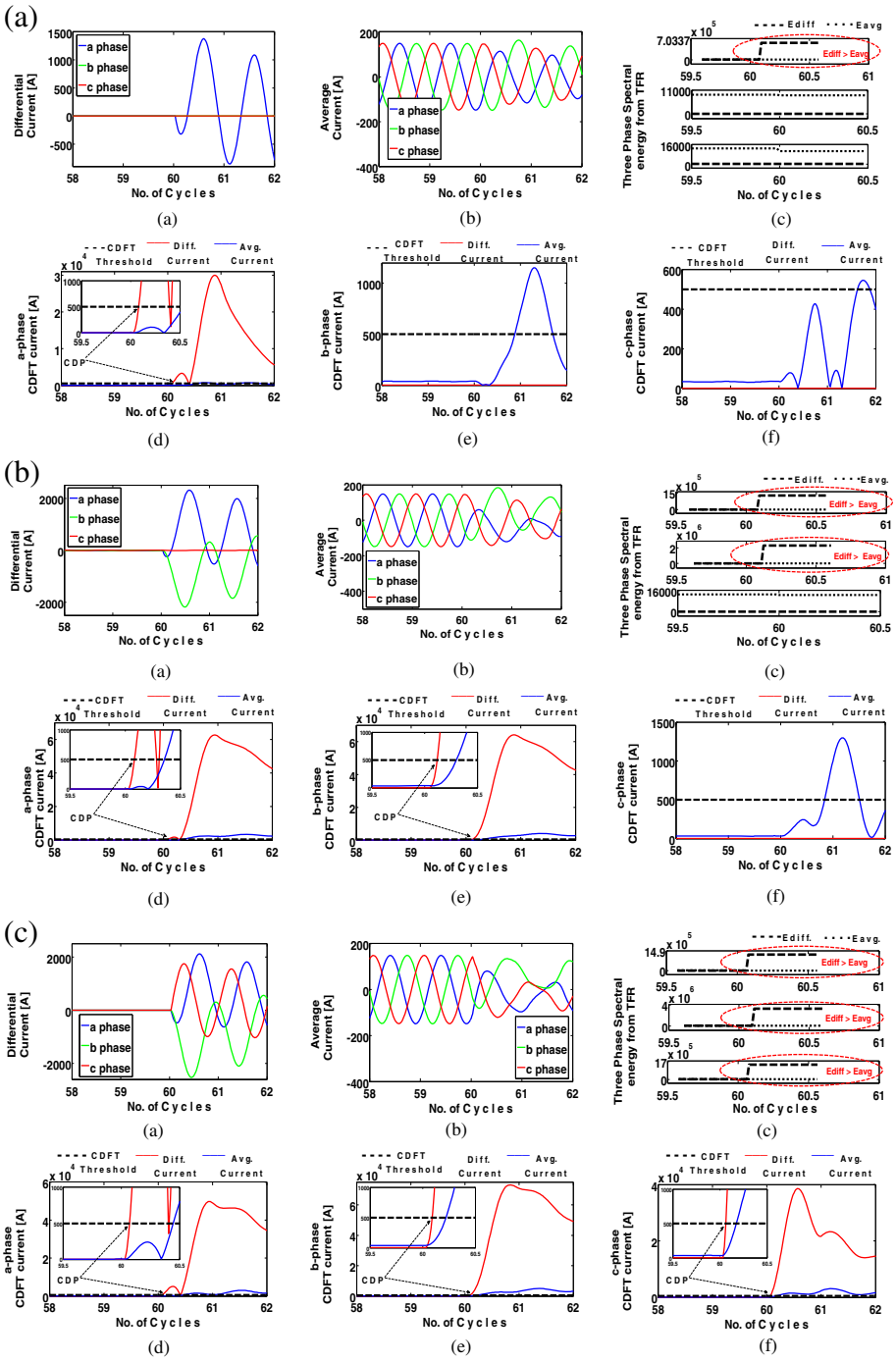

Fig. 2 (See legend on next page.)

(See figure on previous page.)
Fig. 2 a The response of the proposed TFR technique for a *single line* to ground fault (a-g) on the distribution line DLAB with a fault distance ratio (FDR) = 0.5, and fault resistance (Rf) = 1Ω, with the microgrid operating in grid connected mode, where, (*a*) The three phase differential currents, (*b*) The three phase average currents, (*c*) The three phase spectral energy deduced from the proposed TFR technique (Eq. (33)), (*d*) The CDFT over the a-phase differential and average current components, respectively, (*e*) The CDFT over the b-phase differential and average current components, respectively, and (*f*) The CDFT over the c-phase differential and average current components, respectively. **b** The response of the proposed TFR technique for a *double line* to ground fault (ab-g) on the distribution line DLAB with a fault distance ratio (FDR) = 0.5, and fault resistance (Rf) = 1Ω, with the microgrid operating in grid connected mode, where, (*a*) The three phase differential currents, (*b*) The three phase average currents, (*c*) The three phase spectral energy deduced from the proposed TFR technique, (*d*) The CDFT over the a-phase differential and average current components, respectively, (*e*) The CDFT over the b-phase differential and average current components, respectively, and (*f*) The CDFT over the c-phase differential and average current components, respectively. **c** The response of the proposed TFR technique for a *triple line* to ground fault (abc-g) on the distribution *line* DLAB with a fault distance ratio (FDR) = 0.5, and fault resistance (Rf) = 1Ω, with the microgrid operating in grid connected mode, where, (*a*) The three phase differential currents, (*b*) The three phase average currents, (*c*) The three phase spectral energy deduced from the proposed TFR technique, (*d*) The CDFT over the a-phase differential and average current components, respectively, (*e*) The CDFT over the b-phase differential and average current components, respectively, and (*f*) The CDFT over the c-phase differential and average current components, respectively

prominent than the *CDFT* of average current, the occurrence of faults/events is registered. Although *CDFT* inherits a lower computational complexity, but in order to accurately detect the occurrence of the events, a bias setting is always necessary, which alters according the dynamic operating conditions of the network. Thus in order to avoid this, the proposed *TFR* technique is executed over the half cycle values on the both sides of the *CDP* on the average current and the differential current Eq. (23), which generates the respective spectral energy. Various types of faults such as single line to ground fault (*L-g*), double line to ground fault (*LL* and *LL-g*), and single line to ground fault (*LLL* and *LLL-g*) are simulated on different distribution feeders at various locations by varying the fault distance ratio (*FDR*). The *FDR* is considered in p.u. (0–1), i.e., *FDR* of 0.2 for a distribution feeder of length 10 km, with a particular reference point, means a fault at length (0.2 × 10=) 2 km from the reference point on the feeder. Both grid connected mode and the islanded mode operation of the microgrid is considered in this paper. The circuit breaker '*ICB*' is opened to simulate an islanded microgrid, whereas the circuit breakers *CB 1*, *CB 2*, *CB 3*, and *CB 4* are opened to isolate the *DG's*, i.e., *DG 1*, *DG 2*, *DG 3* and *DG 4*, respectively, from the main distribution system.

3.1 Differential spectral energy protection of microgrid subjected to grid connected mode of operation

In order to simulate the *GCM* of operation of the microgrid, the circuit breaker *ICB* is closed for the entire simulation time. Under this mode of operation, depending on the loading conditions, both the DG's as well the utility feed the loads. Thus a fault at a particular location on the distribution feeder will attract current (fault current) from both the DG as well as the utility. The response of the propose *TFR* technique for a single line to ground fault (a-g), a double line to ground fault (ab-g) and a triple line to ground fault (abc-g) simulated at the 60th cycle of the simulation on the distribution line DL_{AB} of the microgrid operating in grid connected mode, and subjected to a fault distance ratio (*FDR*=) 0.5, and fault resistance (R_f=) 1Ω, with are shown in Fig. 2a, b and c, respectively. In these simulations, all the four *DG*'s are connected to the distribution system. The differential current and average current components are shown in the subplots (a) and (b), respectively. In a similar manner, the *CDFT* of the differential and average current components are shown in the subplots (d), (e) and (f), respectively. Finally the three spectral energy of the differential current and average current components are illustrated in the subplot (c). It is observed in these figures that as soon as there is a fault in any of the phases, the differential current (which was nearly zero during normal condition) shoots up, which is quite high as compared to the respective average current component. It is also observed that, the *CDFT* of the differential current is correspondingly very high as compared to the *CDFT* of the average current component plus some bias, and the first instance of occurrence of this condition is registered as *CDP* for the particular phase. Further, it is observed that the type of fault has a significant impact on the fault currents injected by the DG's (in addition to grid currents). The previous statement is clarified in these figures, where the maximum value of differential current is approximately around 1400 A, 2100 A and 2200 A for *L*-g, *LL*-g and *LLL*-g faults respectively. In spite of this, it is observed that the spectral energy of the differential component (E_{diff}) of the corresponding phases exceed the respective spectral energy of the average component (E_{avg}) and hence a fault is detected in almost all the cases simulated. This clearly shows the significance of the proposed TFR method, as it is less vulnerable to the level of DG penetration (i.e., injection of fault current by the DG's) and is a reliable fault detection algorithm for all possible types of faults simulated in this paper. Thus fault detection is based the simple comparison, and the complexity of the bias setting has negligible effect on it (as the magnitude

of E_{diff} is in range of 10^5 which is way more than that of E_{avg} after fault inception).

3.2 Differential spectral energy protection of microgrid subjected to islanded mode of operation

In order to simulate the *IM* of operation of the microgrid, the circuit breaker *ICB* is opened for the entire simulation time. Under this mode of operation, depending on the loading conditions, only the DG's (some portion by the battery bank) will feed the loads. Thus a fault at a particular location on the distribution feeder will attract current (fault current) only from the DG's, which will be smaller as compared to the *GCM* (due to absence of utility). The response of the proposed *TFR* technique for a single line to ground fault (a-g), a double line to ground fault (ab-g) and a triple line to ground fault (abc-g) simulated at the 60th cycle of the simulation on the distribution line DL_{AB} of the microgrid operating in islanded mode, and subjected to a fault distance ratio (*FDR*=) 0.5, and fault resistance (R_f=) 1Ω, with are shown in Figs. 3a, b and c, respectively. In these simulations, all the four *DG*'s are connected to the distribution system. The differential current and average current components are shown in the subplots (a) and (b), respectively. In a similar manner, the *CDFT* of the differential and average current components are shown in the subplots (d), (e) and (f), respectively. Finally the three spectral energy of the differential current and average current components are illustrated in the subplot (c). A similar observation as has been done in the *GCM* of operation of the microgrid is observed from these figure, where the proposed technique is very much efficient in detecting the actual phase of the distribution line under fault under *IM* of operation of the microgrid. In addition, it is observed that the level of the differential and average currents in this mode is considerably lower than the *GCM*, due to the absence of the utility.

3.3 Impact of variation of the DG penetration on the level of differential and average currents

The effect of variation of penetration level of the DG's on the magnitude of the differential and average currents both half cycle before and after the fault inception on the distribution Line DL_{AB} of the microgrid operating in *GCM*, subjected to a single line to ground fault (a-g) and a triple line fault to ground fault (*abc-g*), with *FDR* (0.4 and 0.6) and R_f (5 Ω and 20 Ω), are illustrated in Tables 1 and 2, respectively. Similarly, the effect of variation of penetration level of the DG's on the magnitude of the differential and average currents both half cycle before and after the fault incipient on the distribution Line DL_{AB} of the microgrid operating in *IM*, subjected to single line to ground fault (*a-g*) and a triple line fault to ground fault (abc-g), with *FDR* (0.4 and 0.6) and R_f (5 Ω and 20 Ω) are illustrated in Tables 3 and 4, respectively. In case of maximum value of the half cycle data of the differential currents, it is observed that, the particular phase under fault, its value after fault (as compared to before fault) is very high, for both the GCM as well as the IM of operation of the microgrid, respectively, whereas, for the non-faulted phases, the corresponding values are approximately nearer to each other. It is also observed that, as we decrease the DG penetrations from 'All DG's on' to 'All DG's off', the maximum value of the half cycle data of the differential after fault decreases. For instance, it decreases from 1243.2311 A to 541.5058 A in *GCM* and from 716.5758A to 0.1536 A in *IM* of operation of the microgrid subjected to single line to ground fault (a-g) on distribution line DL_{AB} and which is illustrated in column 4 of Tables 1 and 2, respectively. Similar is the observation for all the other cases in these Tables 1, 2, 3 and 4, respectively. The 'All DG's off', case for the *IM* of operation of the microgrid is intentionally provided in the Table, so as to verify a negligible amount (< 0.2 A, contribution from the of the battery bank) as both the DG's as well as utility do not energize the distribution system. A similar observation is also made for the average currents, where such a high level of difference in the values is seldom observed.

3.4 Classification of internal and external fault

The three phase spectral energy from *TFR* of the differential and average current components for the *GCM* of operation of the microgrid subjected to single phase to ground fault (*a*-g) on distribution line DL_{BC} (with *FDR* 0.3, and R_f = 0.1 Ω), double phase to ground fault (*ab*-g) on distribution line DL_{CD} (with *FDR* 0.5, and R_f = 1 Ω), and triple phase to ground fault (*abc*-g) on distribution line DL_{BE} (with *FDR* 0.7, and R_f = 10 Ω), are shown in Fig. 4a, b and c where the subfigures are denoted as responses for distribution lines (a) DL_{AB}, (b) DL_{AE}, (c) DL_{BE}, (d) DL_{BC} and (e) DL_{CD}, respectively. Similarly, the three phase spectral energy from *TFR* for differential and average current components for the *IM* of operation of the microgrid subjected to single phase to ground fault (*c*-g) on distribution line DL_{AB} (with *FDR* 0.2, and R_f = 0.5 Ω), double phase to ground fault (*bc*-g) on distribution line DL_{BC} (with *FDR* 0.6, and R_f = 5 Ω), and triple phase to ground fault (*abc*-g) on distribution line DL_{AE} (with *FDR* 0.8, and R_f = 20 Ω), are shown in Fig. 5a, b and c, where the subfigures are denoted as responses for distribution lines (a) DL_{AB}, (b) DL_{AE}, (c) DL_{BE}, (d) DL_{BC} and (e) DL_{CD}, respectively.

This section addresses two of the important aspects of the study, i.e., (I) the response of the proposed differential spectral energy protection scheme for different types

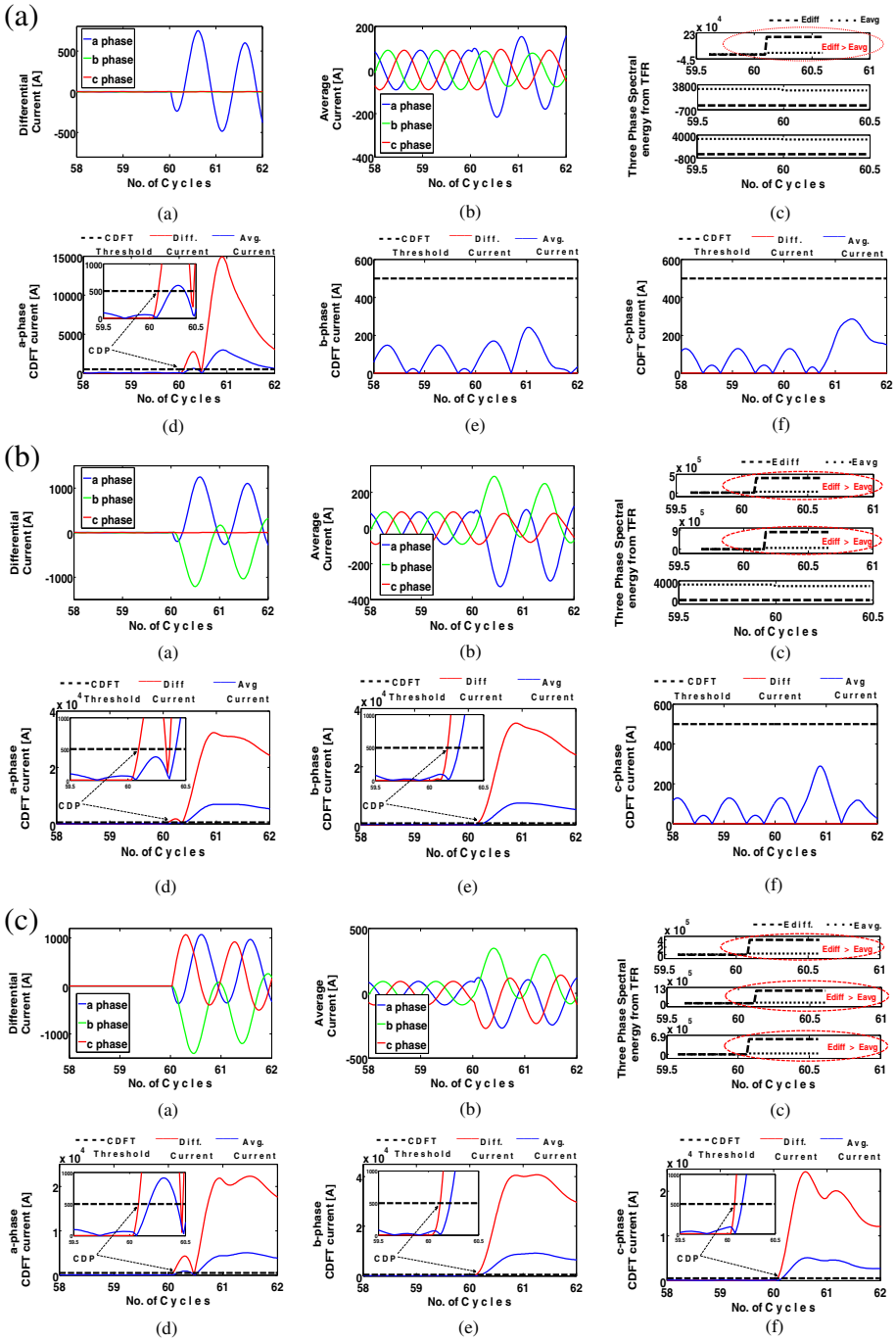

Fig. 3 (See legend on next page.)

(See figure on previous page.)
Fig. 3 a The response of the proposed TFR technique for a single *line* to ground fault (a-g) on the distribution line DLAB with a fault distance ratio (FDR) = 0.5, and fault resistance (Rf) = 1Ω, with the microgrid operating in islanded mode, where, (*a*) The three phase differential currents, (*b*) The three phase average currents, (*c*) The three phase spectral energy deduced from the proposed TFR technique, (*d*) The CDFT over the a-phase differential and average current components, respectively, (*e*) The CDFT over the b-phase differential and average current components, respectively, and (*f*) The CDFT over the c-phase differential and average current components, respectively. **b** The response of the proposed TFR technique for a double line to ground fault (ab-g) on the distribution *line* DLAB with a fault distance ratio (FDR) = 0.5, and fault resistance (Rf) = 1Ω, with the microgrid operating in islanded mode, where, (*a*) The three phase differential currents, (*b*) The three phase average currents, (*c*) The three phase spectral energy deduced from the proposed TFR technique, (*d*) The CDFT over the a-phase differential and average current components, respectively, (*e*) The CDFT over the b-phase differential and average current components, respectively, and (*f*) The CDFT over the c-phase differential and average current components, respectively. **c** The response of the proposed TFR technique for a triple *line* to ground fault (abc-g) on the distribution line DLAB with a fault distance ratio (FDR) = 0.5, and fault resistance (Rf) = 1Ω, with the microgrid operating in islanded mode, where, (*a*) The three phase differential currents, (*b*) The three phase average currents, (*c*) The three phase spectral energy deduced from the proposed TFR technique, (*d*) The CDFT over the a-phase differential and average current components, respectively, (*e*) The CDFT over the b-phase differential and average current components, respectively, and (*f*) The CDFT over the c-phase differential and average current components, respectively

of faults simulated at different distribution lines with different *FDR* and R_f, respectively, and (II) the response of the relays for various types of internal and external faults, both under *GCM* and *IM* of operation of the microgrid, respectively. For elaboration, let us consider Fig. 4a, where it is observed that only one response, i.e., the response for the a- phase of line DL_{BC} satisfies the rule 'Ediff > Eavg + ζ' in the post fault region. For the rest of the responses in this figure, the previous rule does not satisfy, i.e., 'Ediff < Eavg + ζ'. This clearly indicates that the relay at the distribution line DL_{BC} detects an internal *a-g* fault, which lies under its zone of protection, whereas the relay's at other distribution lines do not detect any fault which indicates an external fault lying in a region outside their zone of protection. Similar is the observation for all the figures discussed in this section. Thus it is observed that the proposed method is very much efficient in distinguishing internal and external faults for the relays in the distribution lines, which is effective over a wide range of operating conditions for the microgrid subjected to both *GCM* and *IM* of operation.

Table 1 Effect of variation of penetration level of the DG's on the magnitude of fault current (differential and average) at distribution Line DL_{AB} for a single line to ground fault (a-g) fault on at fault distance ratio (*FDR*) = 0.4 and fault resistance (R_f) = 5 Ω, respectively, where the microgrid is operated in grid connected mode

DG Status	Phase	max (I Differential) (in A)		max (I Average) (in A)	
		Half cycle Before Fault	Half cycle After Fault	Half cycle Before Fault	Half cycle After Fault
All DGs ON	a	0.7887	1243.2311	188.4456	193.2588
	b	0.9299	0.9236	107.5869	193.2588
	c	1.0485	1.2036	136.7399	193.2588
DG1 Off	a	0.8198	987.8662	166.0084	182.2979
	b	0.7250	0.71503	126.1319	182.2979
	c	0.6317	0.6326	254.0888	182.2979
DG1and DG2 Off	a	0.7966	868.9202	235.6965	260.5674
	b	0.7969	0.8156	235.3598	260.5674
	c	0.7963	0.8083	235.4753	260.5674
DG1 DG2 and DG3 Off	a	0.6339	676.7521	287.6676	318.0452
	b	0.6340	0.6613	287.4720	318.0452
	c	0.6343	0.6397	287.2737	318.0452
All DGs OFF	a	0.4761	541.5058	320.6080	350.0915
	b	0.4764	0.4947	320.8868	350.0915
	c	0.4761	0.4719	320.8431	350.0915

Table 2 Effect of variation of penetration level of the DG's on the magnitude of fault current (differential and average) at distribution Line DL_{AB} for a triple line to ground fault (abc-g) fault on at fault distance ratio (FDR) = 0.6 and fault resistance (R_f) = 20 Ω, respectively, where the microgrid is operated in grid connected mode

DG Status	Phase	max (I Differential) (in A)		max (I Average) (in A)	
		Half cycle Before Fault	Half cycle After Fault	Half cycle Before Fault	Half cycle After Fault
All DGs ON	a	0.7879	2181.7049	188.4454	151.6977
	b	0.9295	2359.4328	107.5856	151.6977
	c	1.0478	1751.8088	136.7386	151.6977
DG1 Off	a	0.8203	2033.7771	166.0091	307.9775
	b	0.7245	1890.6872	126.1311	307.9775
	c	0.6321	604.9933	254.0886	307.9775
DG1and DG2 Off	a	0.7954	1313.1837	235.6975	218.5847
	b	0.7957	2083.7611	235.3725	218.5847
	c	0.7951	1575.1316	235.4878	218.5847
DG1 DG2 and DG3 Off	a	0.6325	915.9152	287.6661	286.0211
	b	0.6325	1490.3402	287.4704	286.0211
	c	0.6328	1185.5886	287.2721	286.0211
All DGs OFF	a	0.4747	680.1778	320.6070	320.6017
	b	0.4750	938.8942	320.8858	320.6017
	c	0.4748	757.9855	320.8421	320.6017

Table 3 Effect of variation of penetration level of the DG's on the magnitude of fault current (differential and average) at distribution Line DL_{AB} for a single line to ground fault (a-g) fault on at fault distance ratio (*FDR*) = 0.4 and fault resistance (R_f) = 5 Ω, respectively, where the microgrid is operated in islanded mode

DG Status	Phase	max (I Differential) (in A)		max (I Average) (in A)	
		Half cycle Before Fault	Half cycle After Fault	Half cycle Before Fault	Half cycle After Fault
All DGs ON	a	0.8399	716.5758	0.6071	126.0080
	b	0.8400	0.8638	0.6071	126.0080
	c	0.8401	1.2697	0.6072	126.0080
DG1 Off	a	0.7071	640.5418	70.2472	192.7522
	b	0.7069	0.7275	70.2717	192.7522
	c	0.7070	0.7314	70.2931	192.7522
DG1and DG2 Off	a	0.4701	304.9124	46.2568	95.4453
	b	0.4700	0.4823	46.2104	95.4453
	c	0.4697	0.7155	46.2455	95.4453
DG1 DG2 and DG3 Off	a	0.2332	121.2291	22.6096	39.5804
	b	0.2333	0.2484	22.6212	39.5804
	c	0.2333	0.3317	22.6264	39.5804
All DGs OFF	a	0.0002	0.1536	0.0094	0.0363
	b	0.0002	0.0002	0.0094	0.0363
	c	0.0002	0.0003	0.0094	0.0363

Table 4 Effect of variation of penetration level of the DG's on the magnitude of fault current (differential and average) at distribution Line DL_{AB} for a triple line to ground fault (abc-g) fault, with fault distance ratio (FDR) = 0.6 and fault resistance (R_f) = 20 Ω, respectively, where the microgrid is operated in islanded mode

DG Status	Phase	max (I Differential) (in A)		max (I Average) (in A)	
		Half cycle Before Fault	Half cycle After Fault	Half cycle Before Fault	Half cycle After Fault
All DGs ON	a	0.8399	1716.7085	0.6075	457.5215
	b	0.8400	805.2776	0.6075	457.5215
	c	0.8401	2033.4764	0.6076	457.5215
DG1 Off	a	0.7074	1443.1043	70.2482	492.0391
	b	0.7073	1289.4827	70.2729	492.0391
	c	0.7074	619.6908	70.2943	492.0391
DG1and DG2 Off	a	0.4704	583.9226	46.2576	202.3372
	b	0.4703	661.2137	46.2112	202.3372
	c	0.4699	801.3551	46.2462	202.3372
DG1 DG2 and DG3 Off	a	0.2334	215.5093	22.6099	76.1430
	b	0.2334	315.1619	22.6216	76.1430
	c	0.2334	326.8790	22.6268	76.1430
All DGs OFF	a	0.0002	0.2610	0.0094	0.0779
	b	0.0002	0.2587	0.0094	0.0779
	c	0.0002	0.2800	0.0094	0.0779

3.5 Response of fault location algorithm

As soon as a particular phase of the distribution line is detected with a fault, the measured values of the three phase voltage and current samples (from relay R_{AB}, R_{BE}, R_{AE}, R_{BC} or R_{CD}) are passed through the proposed *TFR* technique, which extracts their fundamental phasor quantities (magnitude and phase angle), respectively, as explained in section II.*D*. Subsequently the fault location ($FL_{estimated}$) as well as the percentage error in fault location are computed.

The response of the fault location algorithm for a single line to ground fault (*a-g*) on distribution line DL_{AB} (with *FDR* 0.6, and R_f = 10 Ω), in the microgrid operating in the *GCM* as well as *IM*, are shown in Fig. 6a and b, respectively. In a similar manner, the response of the fault location algorithm for a triple line to ground fault (*abc-g*) on distribution line DL_{AB} (with *FDR* 0.8, and R_f = 10 Ω), in the microgrid operating in the GCM is shown in Fig. 6c. In all these figures, the subplots are defined as (a) 3-phase voltage signals at the relay R_{AB}, (b) 3-phase current signals at the relay R_{AB}, (c) Resistance (*R* in Ω) seen by the relay R_{AB} through the proposed *TFR* technique in phase 'a,' (c) Reactance (*X* in Ω) seen by the relay R_{AB} through the proposed *TFR* technique in phase 'a,' and (e) R-X trajectory, respectively. It is observed in these figures that, as soon as there is a fault (at the 60th cycle) in any phase of the distribution line DL_{AB}, there are some deviations in the respective three phase voltage and current quantities. It is also observed that, there is a respective steep change/ deviation in the resistance and reactance values. It is further observed that, the estimation done by the conventional *DFT* is not stable, and is oscillatory in the post fault region. On the contrary, the proposed *TFR* technique illustrates a stable and approximate estimation of the resistance and reactance components, respectively. Finally, it is observed that the *R-X* trajectory, for all the cases are well within the zone of protection for faults in both the GCM as well as IM of operation of the microgrid, respectively.

3.6 Impact of variation of DG penetration and FDR on the performance of the fault location algorithm

The impact of the variation of the DG penetrations, on the performance of the proposed fault location algorithm at various.

FDR's is investigated in this section, where Fig. 7 illustrates the comparison of the percentage error in fault location (%) evaluated by the proposed fault location algorithm for single phase to ground fault (*a-g*) at different fault locations (2 km to 18 km i.e., *FDR* varied from 0.1 to 0.9 p.u., respectively), on the distribution line DL_{AB} in the micro grid operating under *GCM*, subjected to various levels of DG penetrations. Further the subplots show the following: (a) response for fault resistance (R_f =) 0.1Ω, (b) response for fault resistance (R_f =) 1Ω, and (c) response for fault resistance (R_f =) 10Ω,

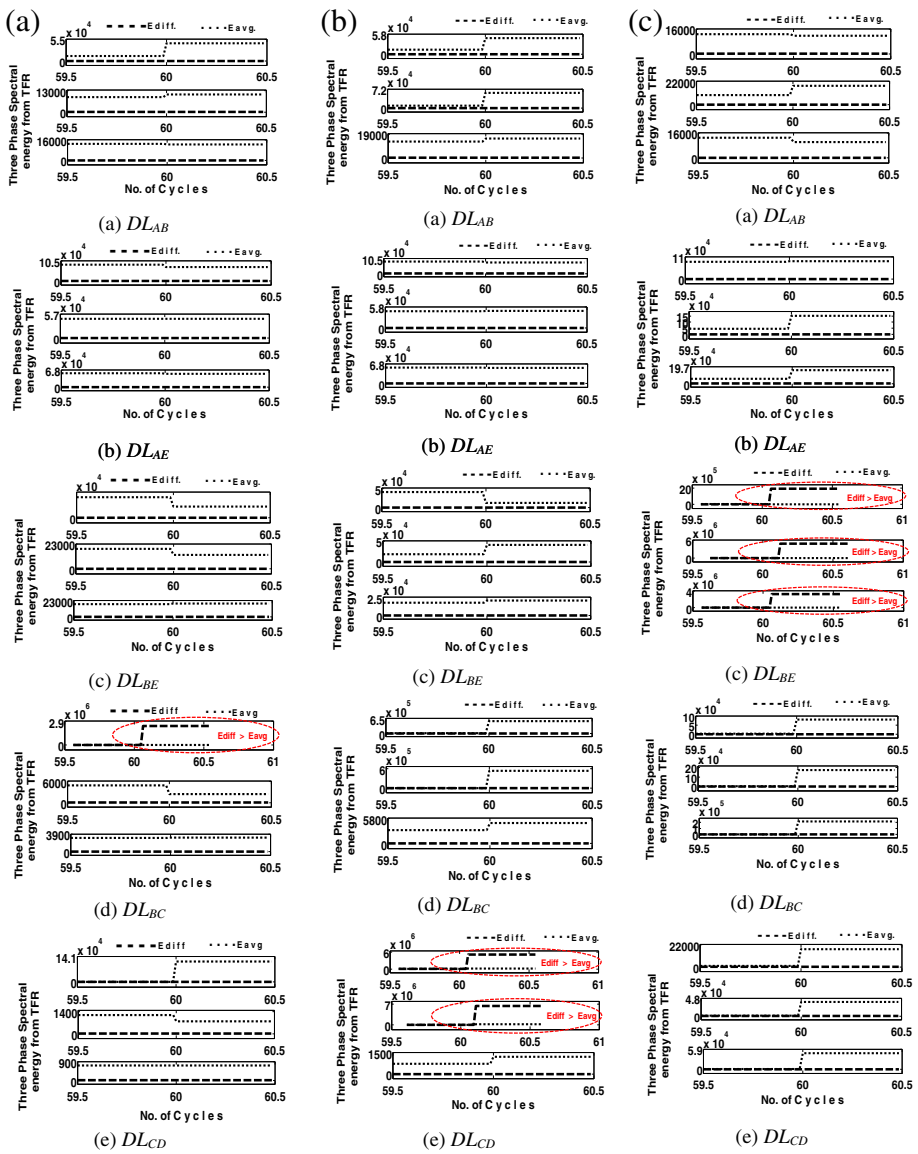

Fig. 4 a The three phase spectral energy from TFR for differential (––) and average (….) currents, for the grid connected microgrid subjected to a single phase to ground fault (a-g) on distribution *line* DLBC (with FDR 0.3, and Rf = 0.1 Ω), where, responses are for distribution lines (*a*) DLAB, (*b*) DLAE, (*c*) DLBE, (*d*) DLBC and (*e*) DLCD, respectively. **b** The three phase spectral energy from TFR for differential (––) and average (….) currents, for the grid connected microgrid subjected to a double phase to ground fault (ab-g) on distribution line DLCD (with FDR 0.5, and Rf = 1 Ω), where, responses are for distribution *lines* (*a*) DLAB, (*b*) DLAE, (*c*) DLBE, (*d*) DLBC and (*e*) DLCD, respectively. **c** The three phase spectral energy from TFR for differential (––) and average (….) currents, for the grid connected microgrid subjected to a triple phase to ground fault (abc-g) on distribution line DLBE (with FDR 0.7, and Rf = 10 Ω), where, responses are for distribution *lines* (*a*) DLAB, (*b*) DLAE, (*c*) DLBE, (*d*) DLBC and (*e*) DLCD, respectively

respectively. In the individual subplots, for most of the cases (except some) it is observed that, the percentage error in fault location (%) for a particular DG penetration increases with increase in *FDR*. It is further observed that, with increase in DG penetration from 'No DG' to 'DG 1234', i.e., from 'No DG on' to 'All DG on', respectively, there is a substantial increase in the percentage error in fault location (%), which is prominent in case of 'DG 1234'. Further, as the fault location algorithm is not dependent on the resistance seen by the relay, it is observed that, with an increase in R_f from 0.1 Ω to 10 Ω, the percentage error in fault location (%), increases for the DG 1234 case with FDR 0.8, respectively. Similar is the observation for all the other cases. Hence it is observed that DG penetration as well as fault distance ratio has significant effect on the accuracy of the proposed fault location technique, which decreases with increase of these quantities, respectively.

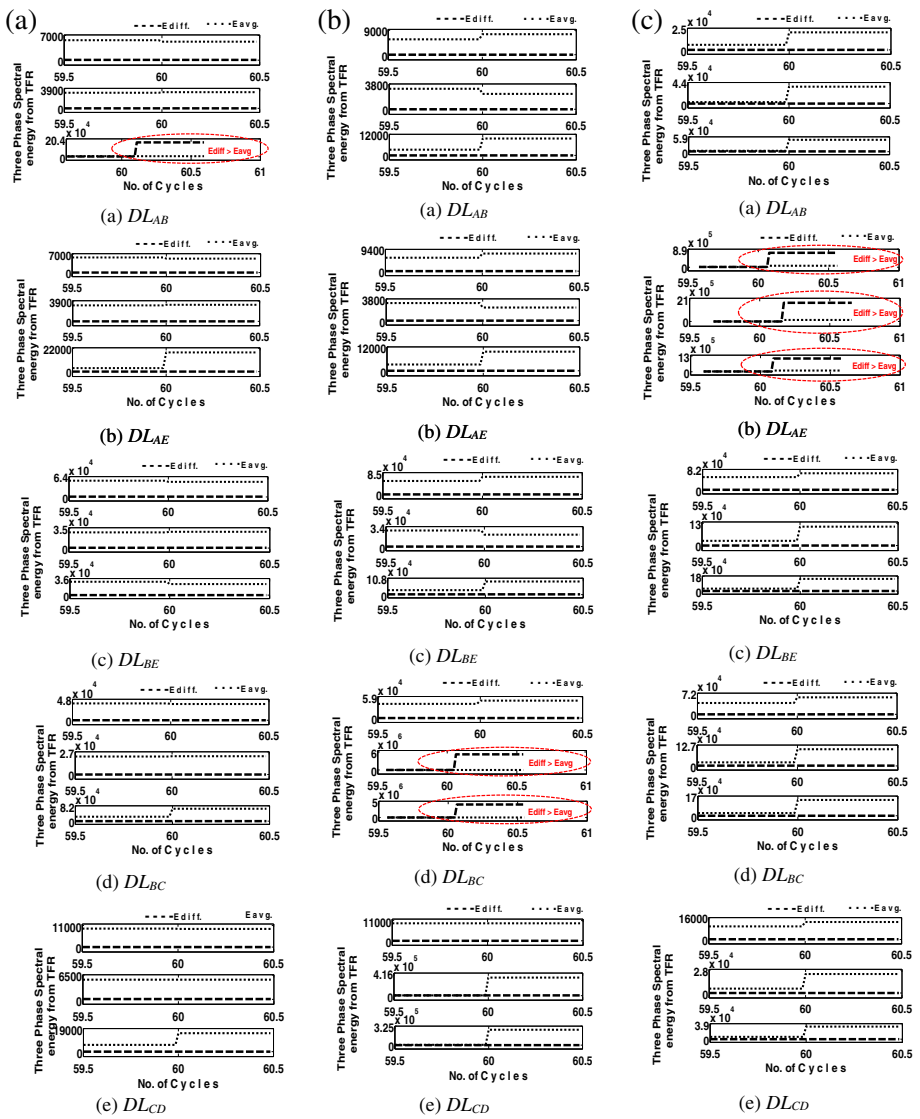

Fig. 5 a The three phase spectral energy from TFR for differential (––) and average (….) currents, for the islanded microgrid subjected to a single phase to ground fault (c-g) on distribution line DLAB (with FDR 0.2, and Rf = 0.5 Ω), where, responses are for distribution *lines* (*a*) DLAB, (*b*) DLAE, (*c*) DLBE, (*d*) DLBC and (*e*) DLCD, respectively. **b** The three phase spectral energy from TFR for differential (––) and average (….) currents, for the islanded microgrid subjected to a double phase to ground fault (bc-g) on distribution line DLBC (with FDR 0.6, and Rf = 5 Ω), where, responses are for distribution lines (*a*) DLAB, (*b*) DLAE, (*c*) DLBE, (*d*) DLBC and (*e*) DLCD, respectively. **c** The three phase spectral energy from TFR for differential (––) and average (….) currents, for the islanded microgrid subjected to a triple phase to ground fault (abc-g) on distribution line DLAE (with FDR 0.8, and Rf = 20 Ω), where, responses are for distribution lines (*a*) DLAB, (*b*) DLAE, (*c*) DLBE, (*d*) DLBC and (*e*) DLCD, respectively

3.7 Relay trip timing for the proposed technique

The time taken by the algorithm to issue a trip signal to the relay, after the instance of fault incipient (*CDP*) is defined as the relay trip time. In the present work, as soon as the fault occurs (just after the completion of the 60th cycle), the proposed *TFR* technique traces for the first instance, where the rule i.e., 'Ediff > Eavg + ζ' is satisfied and correspondingly calculates the time spent for doing so (after fault inception). This time is termed as the relay trip timing (*RTT*), at which a trip signal is issued to the corresponding relay. Table 5 illustrates the comparison of the relay tripping time (in ms) for full cycle window and half cycle window calculations for the microgrid subjected to various types of operating modes (*GCM* and *IM*), fault types, fault resistances, and faulted distribution lines, respectively.

In the full cycle window calculation mode, one complete cycle data (i.e., half cycle data before and half cycle data after the fault incipient) of the E_{diff} and E_{avg} are passed through the *TFR* technique, where as in the half cycle window calculation mode, half cycle data (i.e., quarter cycle data before and quarter cycle data after

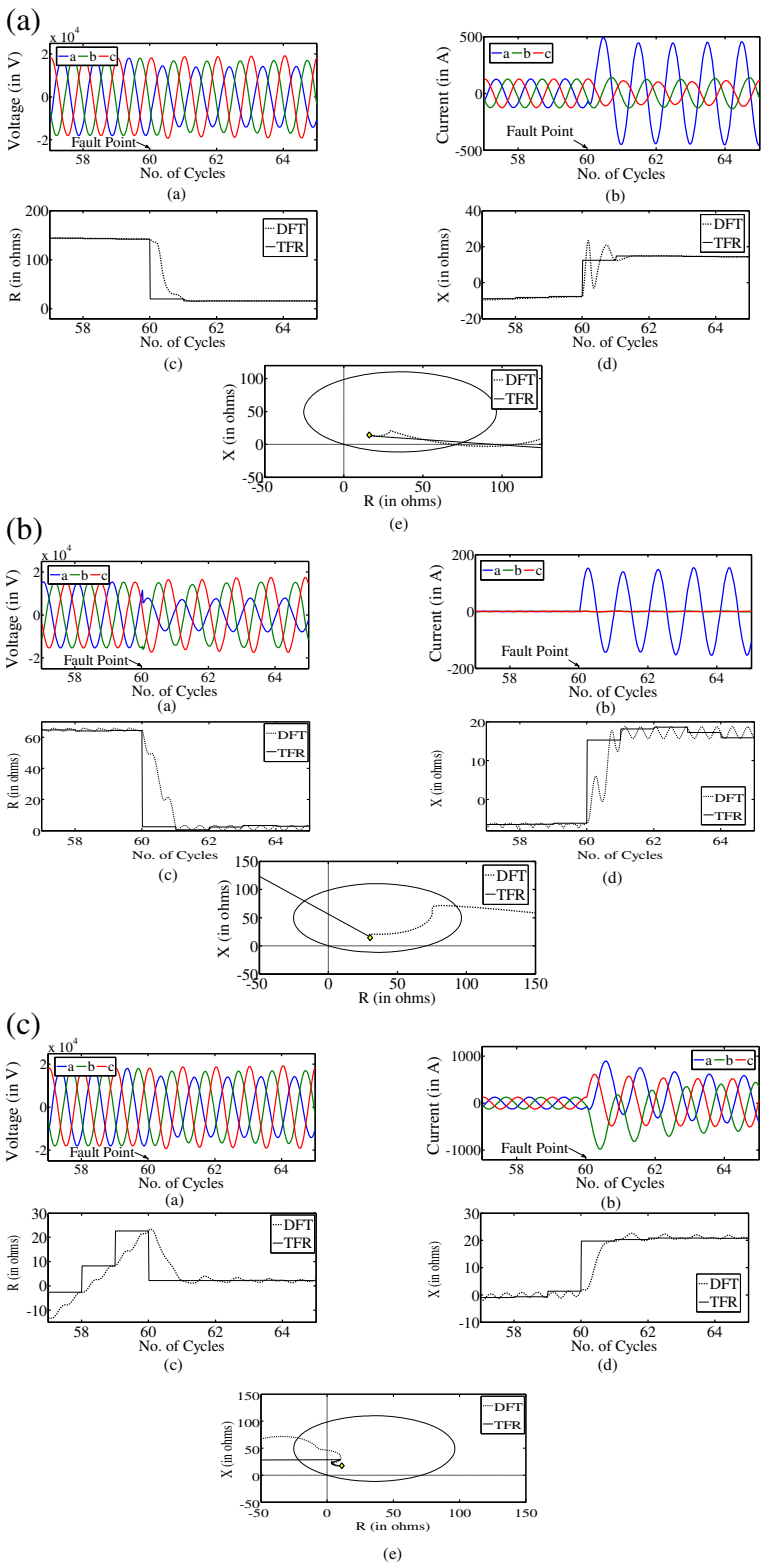

Fig. 6 (See legend on next page.)

(See figure on previous page.)
Fig. 6 a The response of the fault location algorithm on the microgrid operating in the grid connected mode, which is subjected to a single line to ground fault (a-g) on distribution line DLAB (with FDR 0.6, and Rf = 10 Ω), where, (*a*) 3-phase voltage signals at the relay RAB, (*b*) 3-phase current signals at the relay RAB, (*c*) Resistance seen by the relay RAB through the proposed TFR technique in phase 'a', (*d*) Reactance seen by the relay RAB through the proposed TFR technique in phase 'a',, and (*e*) R-X trajectory, respectively. **b** The response of the fault location algorithm on the microgrid operating in the islanded mode, which is subjected to a single *line* to ground fault (a-g) on distribution *line* DLAB (with FDR 0.6, and Rf = 10 Ω), where, (*a*) 3-phase voltage signals at the relay RAB, (*b*) 3-phase current signals at the relay RAB, (*c*) Resistance seen by the relay RAB through the proposed TFR technique in phase 'a', (*d*) Reactance seen by the relay RAB through the proposed TFR technique in phase 'a',, and (*e*) R-X trajectory, respectively. **c** The response of the fault location algorithm on the microgrid operating in the grid connected mode, which is subjected to a three phase to ground fault (abc-g) on distribution *line* DLAB (with FDR 0.8, and Rf = 10 Ω), where, (*a*) 3-phase voltage signals at the relay RAB, (*b*) 3-phase current signals at the relay RAB, (*c*) Resistance seen by the relay RAB through the proposed TFR technique in phase 'a', (*d*) Reactance seen by the relay RAB through the proposed TFR technique in phase 'a',, and (*e*) R-X trajectory, respectively

fault incipient) of the E_{diff} and E_{avg} are passed through the *TFR* technique, for the calculation of the relay trip timing. It is observed that, in full cycle window mode, the *RTT* for corresponding phase of the distribution line under fault is obtained within one cycle (20 *ms*) of fault incipient. It is also significant to note that, while in half cycle window mode, as we process nearly half the samples, thus *RTT* is obtained within 10 ms (except row 29), i.e., within half cycle from the fault inception time. Thus two significant contributions can be outlined from this section, (*i*) Utilization of half cycle window mode, instead of full cycle window mode, extracts the *RTT* well within half cycle of fault incipient, thus we overcome the problem of CT saturation as outlined in [19] as well as obtain quick *RTT* response as compared to [17], respectively; and (ii) regardless of the large combination of operating points, the proposed technique is significantly successful for almost all of them, which validates the applicability of the proposed *TFR* technique under wide range of operating points.

3.8 Performance evaluation of the proposed technique

Tables 6, 7 and 8 illustrate the comparison for the estimated fault distance (km) and percentage error in fault location (*PEFL*) for a single line to ground fault (a-g) on the distribution line DL_{AB} in the micro grid operating under *GCM*, at different fault locations (2 km to 18 km i.e., *FDR* varied from 0.1 to 0.9 p.u., respectively), with fault resistance's (R_f =) 0.1Ω, 1Ω and 10 Ω, and the microgrid subjected to various levels of DG penetrations, respectively. It is to be noted that, the above propositions have been verified under all the operating conditions discussed in the previous sections, but only one case study has been presented to reduce the length of the manuscript. Let us consider the case of higher DG penetration, i.e., where DG 1, 2, 3, 4 are on, i.e., connected to the microgrid. It is observed in these tables that for R_f = 0.1 Ω case, as we increase the *FDR* from 0.1 p.u. to 0.9 p.u., the *PEFL* (%) increases from (0.0622 vs 0.3412) % to 1.6334 vs 18.488) %, for the (proposed TFR vs conventional DFT) techniques, respectively.

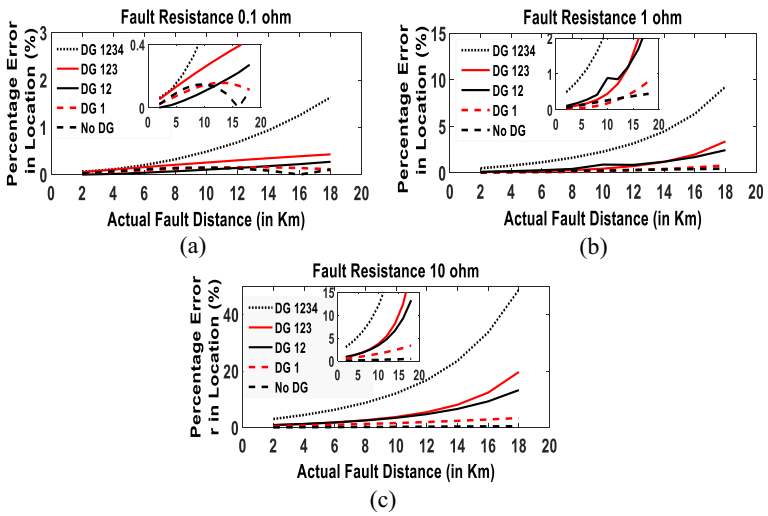

Fig. 7 Comparison of the percentage error in fault location (%) evaluated by the proposed fault location algorithm for single phase to ground fault (a-g) at different fault locations (2 Km to 18 Km i.e., FDR varied from 0.1 to 0.9 p.u., respectively), on the distribution *line* DLAB in the micro grid operating under grid connected mode, subjected to various levels of DG penetrations, where (**a**) response for fault resistance (Rf =) 0.1Ω, (**b**) response for fault resistance (Rf) = 1Ω, and (**c**) response for fault resistance (Rf) = 10Ω, respectively

Table 5 Comparison of the relay trip timings (in ms) for full cycle window and half cycle window calculations for the microgrid subjected to various types of operating modes (GCM and IM), fault types, fault resistances, and faulted distribution lines, respectively

Sl. no.	Microgrid operation mode	Fault Type	Fault Resistance (in Ω)	Fault Distance Ratio (0–1) [×100] in %	Faulted Line	Relay trip timing (in ms) Full Window Calculation			Relay trip timing (in ms) Half Window Calculation		
						Phase a	Phase b	Phase c	Phase a	Phase b	Phase c
1	*GCM (DG 1234 ON)*	*a-g*	0.1	0.8	DL_{AB}	10.6771	-	-	6.5104	-	-
2		*b-g*	1	0.7		-	9.8958	-	-	5.7292	-
3		*c-g*	10	0.6		-	-	9.8958	-	-	5.7292
4		*ab-g*	0.1	0.5	DL_{AE}	10.9375	10.4167	-	6.7708	6.2500	-
5		*bc-g*	1	0.4		-	10.1563	9.8958	-	5.9896	5.7292
6		*ca-g*	10	0.3		12.2396	-	9.8958	8.0729	-	5.7292
7		*abc-g*	0.1	0.2	DL_{BE}	10.9375	10.1563	9.3750	6.7708	5.9896	5.2083
8		*abc-g*	1	0.1		10.6771	9.8958	9.3750	6.5104	5.7292	5.2083
9		*abc-g*	10	0.5		10.9375	10.4167	9.8958	6.7708	6.2500	5.7292
10	*GCM (DG 1234 OFF)*	*a-g*	0.1	0.1	DL_{AB}	9.8958	-	-	5.7292	-	-
11		*b-g*	1	0.2		-	9.8958	-	-	5.7292	-
12		*c-g*	10	0.3		-	-	9.6354	-	-	5.4687
13		*ab-g*	0.1	0.4	DL_{AE}	10.6771	10.1563	-	6.5104	5.9896	-
14		*bc-g*	1	0.5		-	9.8958	9.6354	-	5.7292	5.4687
15		*ca-g*	10	0.6		9.6354	-	9.6354	5.4687	-	5.4687
16		*abc-g*	0.1	0.7	DL_{BE}	9.8958	10.6771	9.6354	5.7292	6.5104	5.4687
17		*abc-g*	1	0.8		9.8958	10.4167	9.6354	5.7292	6.2500	5.4687
18		*abc-g*	10	0.5		9.6354	10.9375	9.6354	5.4687	6.7708	5.4687
19	*IM (DG 1234 ON)*	*a-g*	0.1	0.1	DL_{BC}	13.0208	-	-	8.8542	-	-
20		*b-g*	1	0.2		-	10.1563	-	-	5.9896	-
21		*c-g*	10	0.3		-	-	11.4583	-	-	7.2917
22		*ab-g*	0.1	0.4	DL_{CD}	9.8958	9.1146	-	5.7292	4.9479	-
23		*bc-g*	1	0.5		-	9.1146	9.1146	-	4.9479	4.9479
24		*ca-g*	10	0.6		11.4583	-	9.6354	7.2917	-	5.4687
25		*abc-g*	0.1	0.7	DL_{BE}	12.7604	9.8958	9.6354	8.5937	5.7292	5.4687
26		*abc-g*	1	0.8		12.7604	9.8958	9.6354	8.5937	5.7292	5.4687
27		*abc-g*	10	0.5		12.5000	9.8958	9.6354	8.3333	5.7292	5.4687
28	*IM (DG 1*	*a-g*	0.1	0.8	DL_{BC}	11.1979	-	-	7.0313	-	-

Table 5 Comparison of the relay trip timings (in ms) for full cycle window and half cycle window calculations for the microgrid subjected to various types of operating modes (GCM and IM), fault types, fault resistances, and faulted distribution lines, respectively *(Continued)*

29	*ON)*	*b-g*	1	0.7		-	14.8438	-	-	10.6771	-
30		*c-g*	10	0.6		-	-	11.1979	-	-	7.0313
31		*ab-g*	0.1	0.5	DL_{CD}	11.1979	10.4167	-	7.0313	6.2500	-
32		*bc-g*	1	0.4		-	10.4167	9.8958	-	6.2500	5.7292
33		*ca-g*	10	0.3		10.4167	-	10.4167	6.25	-	6.25
34		*abc-g*	0.1	0.2	DL_{BE}	10.1563	9.6354	10.1563	5.9896	5.4687	5.9896
35		*abc-g*	1	0.1		9.8958	9.6354	10.1563	5.7292	5.7292	5.7292
36		*abc-g*	10	0.5		13.5417	9.8958	10.1563	9.375	5.7292	5.9896

Table 6 Comparison for the estimated fault distance (km) and percentage error in fault location (%) for a single line to ground fault (a-g), with a fault resistance (R_f) = 0.1Ω at different fault locations (2 km to 18 km i.e., *FDR* varied from 0.1 to 0.9 p.u., respectively), on the distribution line DL_{AB} in the micro grid operating under grid connected mode, subjected to various levels of DG penetrations

l. No.	Fault Type	Fault Resistance (in Ω)	Fault Distance Ratio (0–1) [×100 in %]	Faulted Distribution Line	Total line Distance (in km)	Actual Fault Distance (km)	DG status	Conventional DFT Technique		Proposed *TFR* technique	
								Estimate (km)	Percentage Error in Fault Location (in %)	Estimate (km)	Percentage Error in Fault Location (in %)
1	a-g	0.1	0.1	DL_{AB}	20	2	DG 1 2 3 4 on	2.0681	0.3412	2.0112	0.0622
2			0.2	L_{AB}	20	4		4.0944	0.4731	4.0226	0.1121
3			0.3	L_{AB}	20	6		6.1261	0.6353	6.0400	0.2024
4			0.4	L_{AB}	20	8		8.1639	0.8254	8.0640	0.3243
5			0.5	L_{AB}	20	10		10.208	1.0412	10.095	0.4863
6			0.6	L_{AB}	20	12		12.2614	1.3114	12.1360	0.6826
7			0.7	L_{AB}	20	14		14.3241	1.6262	14.1866	0.9376
8			0.8	L_{AB}	20	16		16.3989	1.9959	16.2495	1.2522
9			0.9	L_{AB}	20	18		18.4888	2.4421	18.3258	1.6334
10			0.1	L_{AB}	20	2	DG 1 2 3 on DG 4 off	2.0436	0.2180	1.9892	0.0542
11			0.2	L_{AB}	20	4		4.0479	0.2395	3.9785	0.1076
12			0.3	L_{AB}	20	6		6.0527	0.2633	5.9681	0.1594
13			0.4	L_{AB}	20	8		8.0580	0.2902	7.9581	0.2097
14			0.5	L_{AB}	20	10		10.0640	0.3198	9.9485	0.2577
15			0.6	L_{AB}	20	12		12.0705	0.3525	11.9393	0.3034
16			0.7	L_{AB}	20	14		14.0777	0.3886	13.9305	0.3475
17			0.8	L_{AB}	20	16		16.0857	0.4283	15.9221	0.3897
18			0.9	L_{AB}	20	18		18.0944	0.4721	17.9140	0.4300
19			0.1	L_{AB}	20	2	DG 1 2 on DG 3 4 off	2.0283	0.1415	2.0004	0.0018
20			0.2	L_{AB}	20	4		4.0364	0.1820	4.0033	0.0167
21			0.3	L_{AB}	20	6		6.0458	0.2289	6.0083	0.0413
22			0.4	L_{AB}	20	8		8.0557	0.2786	8.0143	0.0717
23			0.5	L_{AB}	20	10		10.0660	0.3302	10.0212	0.1059
24			0.6	L_{AB}	20	12		12.0766	0.3830	12.0285	0.1425
25			0.7	L_{AB}	20	14		14.0873	0.4365	14.0362	0.1809
26			0.8	L_{AB}	20	16		16.0985	0.4923	16.0445	0.2225
27			0.9	L_{AB}	20	18		18.1110	0.5551	18.0546	0.2730
10			0.1	L_{AB}	20	2	DG 1 on DG 2 3 4 off	2.0506	0.2531	1.9950	0.0248
11			0.2	L_{AB}	20	4		4.0600	0.3001	3.9884	0.0582

Table 6 Comparison for the estimated fault distance (km) and percentage error in fault location (%) for a single line to ground fault (a-g), with a fault resistance (R_f) = 0.1Ω at different fault locations (2 km to 18 km i.e., *FDR* varied from 0.1 to 0.9 p.u., respectively), on the distribution line DL_{AB} in the micro grid operating under grid connected mode, subjected to various levels of DG penetrations *(Continued)*

12	0.3	L_{AB}	20	6		6.0694	0.3470	5.9816	0.0922
13	0.4	L_{AB}	20	8		8.0793	0.3963	7.9756	0.1221
14	0.5	L_{AB}	20	10		10.0903	0.4514	9.9710	0.1450
15	0.6	L_{AB}	20	12		12.1030	0.5150	11.9684	0.1579
16	0.7	L_{AB}	20	14		14.1183	0.5917	13.9685	0.1576
17	0.8	L_{AB}	20	16		16.1370	0.6850	15.9718	0.1411
18	0.9	L_{AB}	20	18		18.1584	0.7922	17.9770	0.1150
19	0.1	L_{AB}	20	2	DG 1 2 3 4 off	2.0226	0.1130	2.0045	0.0227
20	0.2	L_{AB}	20	4		4.0309	0.1545	4.0145	0.0723
21	0.3	L_{AB}	20	6		6.0371	0.1853	6.0231	0.1154
22	0.4	L_{AB}	20	8		8.0397	0.1983	8.0286	0.1431
23	0.5	L_{AB}	20	10		10.0379	0.1893	10.0300	0.1499
24	0.6	L_{AB}	20	12		12.0310	0.1548	12.0266	0.1328
25	0.7	L_{AB}	20	14		14.0184	0.0922	14.0174	0.0871
26	0.8	L_{AB}	20	16		16.0019	0.0094	15.9995	0.0025
27	0.9	L_{AB}	20	18		17.9733	0.1335	17.9787	0.1065

Table 7 Comparison for the estimated fault distance (km) and percentage error in fault location (%) for a single line to ground fault (a-g), with a fault resistance (R_f) = 1Ω at different fault locations (2 km to 18 km i.e., *FDR* varied from 0.1 to 0.9 p.u., respectively), on the distribution line DL_{AB} in the micro grid operating under grid connected mode, subjected to various levels of DG penetrations

Sl. No.	Fault Type	Fault Resistance (in Ω)	Fault Distance Ratio (0–1) [×100 in %]	Faulted Distribution Line	Total line Distance (in km)	Actual Fault Distance (km)	DG status	Conventional DFT Technique		Proposed *TFR* technique	
								Estimate (km)	Percentage Error (in %)	Estimate (km)	Percentage Error (in %)
1	a-g	1	0.1	L_{AB}	20	2	DG 1 2 3 4 on	2.1541	0.7768	2.0984	0.4912
2			0.2	L_{AB}	20	4		4.2222	1.1121	4.1536	0.7726
3			0.3	L_{AB}	20	6		6.3076	1.5457	6.2266	1.1372
4			0.4	L_{AB}	20	8		8.4156	2.0833	8.3233	1.6240
5			0.5	L_{AB}	20	10		10.5556	2.7839	10.4533	2.2747
6			0.6	L_{AB}	20	12		12.7426	3.7161	12.6322	3.1629
7			0.7	L_{AB}	20	14		15.0035	5.0289	14.8872	4.4484
8			0.8	L_{AB}	20	16		17.3870	6.9461	17.2666	6.3363
9			0.9	L_{AB}	20	18		19.9789	9.8962	19.8504	9.2559
10			0.1	L_{AB}	20	2	DG 1 2 3 on DG 4 off	2.0704	0.3519	2.0154	0.0771
11			0.2	L_{AB}	20	4		4.0932	0.4661	4.0235	0.1175
12			0.3	L_{AB}	20	6		6.1206	0.6030	6.0359	0.1795
13			0.4	L_{AB}	20	8		8.1555	0.7777	8.0563	0.2813
14			0.5	L_{AB}	20	10		10.2029	1.0146	10.0896	0.4479
15			0.6	L_{AB}	20	12		12.2711	1.3557	12.1445	0.7223
16			0.7	L_{AB}	20	14		14.3753	1.8764	14.2358	1.1792
17			0.8	L_{AB}	20	16		16.5453	2.7266	16.3933	1.9666
18			0.9	L_{AB}	20	18		18.8441	4.2204	18.6763	3.3816
19			0.1	L_{AB}	20	2	DG 1 2 on DG 3 4 off	2.0546	0.2732	2.0218	0.1091
20			0.2	L_{AB}	20	4		4.0754	0.3769	4.0360	0.1800
21			0.3	L_{AB}	20	6		6.1019	0.5096	6.0565	0.2826
22			0.4	L_{AB}	20	8		8.1353	0.6766	8.0842	0.4210
23			0.5	L_{AB}	20	10		10.1775	0.8876	10.1775	0.8876
24			0.6	L_{AB}	20	12		12.2326	1.1631	12.1705	0.8527
25			0.7	L_{AB}	20	14		14.3069	1.5347	14.2395	1.1973
26			0.8	L_{AB}	20	16		16.4116	2.0580	16.3388	1.6940
27			0.9	L_{AB}	20	18		18.5654	2.8269	18.4883	2.4416
10			0.1	L_{AB}	20	2	DG 1 on DG 2 3 4 off	1.9689	0.1557	1.9951	0.0244
11			0.2	L_{AB}	20	4		3.9648	0.1759	3.9921	0.0396

Table 7 Comparison for the estimated fault distance (km) and percentage error in fault location (%) for a single line to ground fault (a-g), with a fault resistance (R_f) = 1Ω at different fault locations (2 km to 18 km i.e., *FDR* varied from 0.1 to 0.9 p.u., respectively), on the distribution line DL_{AB} in the micro grid operating under grid connected mode, subjected to various levels of DG penetrations *(Continued)*

12	0.3	L_{AB}	20	6		5.9595	0.2026	5.9871	0.0645
13	0.4	L_{AB}	20	8		7.9505	0.2476	7.9781	0.1094
14	0.5	L_{AB}	20	10		9.9364	0.3179	9.9641	0.1793
15	0.6	L_{AB}	20	12		11.9163	0.4184	11.9443	0.2787
16	0.7	L_{AB}	20	14		13.8891	0.5544	13.9177	0.4116
17	0.8	L_{AB}	20	16		15.8536	0.7321	15.8836	0.5820
18	0.9	L_{AB}	20	18		17.8085	0.9573	17.8410	0.7948
19	0.1	L_{AB}	20	2	DG 1 2 3 4 off	2.0448	0.2238	1.9892	0.0542
20	0.2	L_{AB}	20	4		4.0488	0.2441	3.9784	0.1079
21	0.3	L_{AB}	20	6		6.0534	0.2671	5.9677	0.1613
22	0.4	L_{AB}	20	8		8.0586	0.2929	7.9574	0.2132
23	0.5	L_{AB}	20	10		10.0643	0.3213	9.9473	0.2635
24	0.6	L_{AB}	20	12		12.0706	0.3529	11.9375	0.3123
25	0.7	L_{AB}	20	14		14.0775	0.3875	13.9282	0.3591
26	0.8	L_{AB}	20	16		16.0852	0.4259	15.9191	0.4044
27	0.9	L_{AB}	20	18		18.0937	0.4687	17.9105	0.4474

Table 8 Comparison for the estimated fault distance (km) and percentage error in fault location (%) for a single line to ground fault (a-g), with a fault resistance (R_f) = 10 Ω at different fault locations (2 km to 18 km i.e., *FDR* varied from 0.1 to 0.9 p.u., respectively), on the distribution line DL_{AB} in the micro grid operating under grid connected mode, subjected to various levels of DG penetrations

l. No.	Fault Type	Fault Resistance (in Ω)	Fault Distance Ratio (0–1) [×100 in %]	Faulted Distribution Line	Total line Distance (in km)	Actual Fault Distance (km)	DG status	Conventional DFT Technique		Proposed *TFR* technique	
								Estimate (km)	Percentage Error (in %)	Estimate (km)	Percentage Error (in %)
1	a-g	10	0.1	L_{AB}	20	2	DG 1 2 3 4 on	2.6584	3.2919	2.6063	3.0313
2			0.2	L_{AB}	20	4		4.9467	4.7335	4.8906	4.4529
3			0.3	L_{AB}	20	6		7.3169	6.5844	7.2603	6.3014
4			0.4	L_{AB}	20	8		9.8024	9.0119	9.7498	8.7491
5			0.5	L_{AB}	20	10		12.4584	12.2922	12.4164	12.0822
6			0.6	L_{AB}	20	12		15.3774	16.8869	15.3552	16.7761
7			0.7	L_{AB}	20	14		18.7261	23.6306	18.7162	23.5808
8			0.8	L_{AB}	20	16		22.7886	33.9430	22.7344	33.6720
9			0.9	L_{AB}	20	18		27.8364	49.1818	27.7534	48.7672
10			0.1	L_{AB}	20	2	DG 1 2 3 on DG 4 off	2.2228	1.1139	2.1697	0.8484
11			0.2	L_{AB}	20	4		4.3147	1.5736	4.2531	1.2655
12			0.3	L_{AB}	20	6		6.4357	2.1787	6.3664	1.8321
13			0.4	L_{AB}	20	8		8.5999	2.9993	8.5240	2.6198
14			0.5	L_{AB}	20	10		10.8311	4.1557	10.7506	3.7530
15			0.6	L_{AB}	20	12		13.1717	5.8587	13.0889	5.4445
16			0.7	L_{AB}	20	14		15.6986	8.4931	15.6156	8.0778
17			0.8	L_{AB}	20	16		18.5583	12.7917	18.4735	12.3675
18			0.9	L_{AB}	20	18		22.0391	20.1955	21.9325	19.6624
19			0.1	L_{AB}	20	2	DG 1 2 on DG 3 4 off	2.2391	1.1954	2.1821	0.9105
20			0.2	L_{AB}	20	4		4.3287	1.6434	4.2578	1.2891
21			0.3	L_{AB}	20	6		6.4452	2.2262	6.3608	1.8039
22			0.4	L_{AB}	20	8		8.5982	2.9912	8.4996	2.4982
23			0.5	L_{AB}	20	10		10.8020	4.0101	10.6882	3.4411
24			0.6	L_{AB}	20	12		13.0794	5.3970	12.9491	4.7454
25			0.7	L_{AB}	20	14		15.4663	7.3316	15.3185	6.5924
26			0.8	L_{AB}	20	16		18.0207	10.1035	17.8542	9.2712
27			0.9	L_{AB}	20	18		20.8351	14.1755	20.6508	13.2541
10			0.1	L_{AB}	20	2	DG 1 on DG 2 3 4 off	1.8329	0.8355	1.9015	0.4927
11			0.2	L_{AB}	20	4		3.7707	1.1467	3.8521	0.7395

Table 8 Comparison for the estimated fault distance (km) and percentage error in fault location (%) for a single line to ground fault (a-g), with a fault resistance (R_f) = 10 Ω at different fault locations (2 km to 18 km i.e., *FDR* varied from 0.1 to 0.9 p.u., respectively), on the distribution line DL_{AB} in the micro grid operating under grid connected mode, subjected to various levels of DG penetrations *(Continued)*

12	0.3	L_{AB}	20	6		5.7063	1.4684	5.8006	0.9971
13	0.4	L_{AB}	20	8		7.6361	1.8194	7.7438	1.2809
14	0.5	L_{AB}	20	10		9.5573	2.2137	9.6798	1.6011
15	0.6	L_{AB}	20	12		11.4676	2.6620	11.6070	1.9652
16	0.7	L_{AB}	20	14		13.3650	3.1751	13.5239	2.3803
17	0.8	L_{AB}	20	16		15.2473	3.7635	15.4295	2.8525
18	0.9	L_{AB}	20	18		17.1122	4.4392	17.3225	3.3877
19	0.1	L_{AB}	20	2	DG 1 2 3 4 off	2.0501	0.2504	1.9889	0.0553
20	0.2	L_{AB}	20	4		4.0535	0.2677	3.9780	0.1099
21	0.3	L_{AB}	20	6		6.0576	0.2880	5.9673	0.1637
22	0.4	L_{AB}	20	8		8.0622	0.3110	7.9565	0.2174
23	0.5	L_{AB}	20	10		10.0674	0.3371	9.9460	0.2701
24	0.6	L_{AB}	20	12		12.0733	0.3664	11.9356	0.3219
25	0.7	L_{AB}	20	14		14.0798	0.3990	13.9256	0.3722
26	0.8	L_{AB}	20	16		16.0871	0.4356	15.9157	0.4214
27	0.9	L_{AB}	20	18		18.0953	0.4764	17.9063	0.4686

Similarly, for R_f = 1 Ω and 10 Ω cases, as we increase the fault distance ratio from 0.1 p.u. to 0.9 p.u., the percentage error in fault location (%) increases from (0.4912 vs 0.7768) % to 9.2559 vs 19.9789) %, and from (3.0313 vs 3.2919) % to 48.7672 vs 49.1818) %, for the (proposed *TFR* vs conventional *DFT*) techniques, respectively. Similar observations are also observed for all the other cases illustrated in these figures. It is further observed that, with the increases in DG penetration or increases in R_f, the difference between *PEFL* (%) exhibited by proposed *TFR* vs conventional *DFT* techniques, respectively, slightly decreases. In spite of that, it is very much clear from all the observations that, the proposed TFR technique illustrates a better fault location algorithm exhibiting the lower *PEFL* (%) in almost all the cases illustrated in the Tables 6, 7 and 8. This proves the significance and advantage of the proposed TFR technique over the conventional DFT technique.

3.9 Effect of post fault dynamic response of DGs

Since with the spectral energy protection scheme the trip sinal is generated within one cycle and therefore this transient will have practically no effects on the converters connected to DGs. ince thisdigital scheme is very fast the fault current limiting on the converter side will not influence on the protection algorithms. For illustration the pre and post fault dynamic response of the DG 1 in the proposed microgrid model, which is subjected to a double line to ground fault in DL_{AB} (with *FDR* = 0.5) at 60th cycle of simulation which lasts for 13 cycle, i.e., fault cleared at 73th cycle, and the voltage and current waveforms at the DG 1 terminal after the transformer connection areshown in Fig. 8. From the results it is quite clear the voltage and current waveforms come to their initial values very quickly after the fault is cleared.

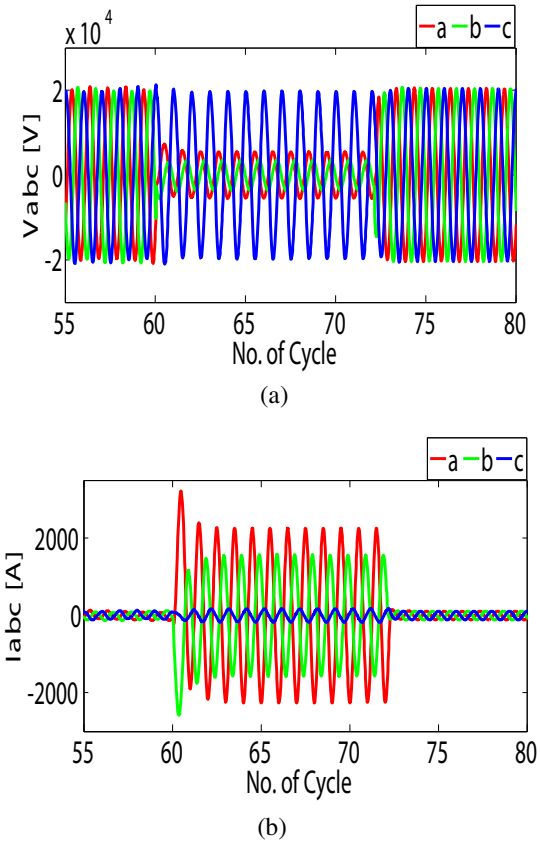

Fig. 8 Pre and Post Fault dynamic response of DG1. **a** Voltage at DG1 terminal after transformer. **b** Current at the DG1 terminal after transformer

4 Conclusion

This paper investigates a fast and accurate pattern recognition technique (Sparse Fourier kernel based fast time-frequency representation) based differential spectral energy protection approach for an ac microgrid. In this regard, the first instant of fault inception is initially traced using a change detection (characterized by *CDP*) filter technique over the differential and average current components. In order to avoid a large computational overhead by processing large number of data samples, only one cycle or half cycle data (half of data from either side of the *CDP*) are passed through the proposed *TFR* technique, which significantly reduces its computational burden. In comparison to threshold setting based conventional differential protection techniques; the proposed scheme illustrates a better performance, with much reduced relay trip timings (less than half cycle) and is very much immune to the threshold setting. Further, the impact of variation of a large number of operating conditions such as mode of operation of the microgrid (grid connected or islanded), type of fault ((single line to ground faults (*L*-g), double line to ground faults (*LL*-g), and triple line to ground fault (*LLL*-g), fault resistance, fault distance ratio, and the level of penetration of the DG, respectively, on the performance of the proposed technique has been extensively verified on a standard distribution generation (DFIG wind farm) based ac microgrid, which has been simulated in the MATLAB/ Simulink environment. The proposed technique as compared to conventional *DFT* and differential current based protection scheme, has a number of advantages, such as reduced computational complexity, reduced effect of bias setting for fault detection, quicker fault detection and classification, better accuracy of fault location and a faster relay response time (less than half cycle). This has been illustrated in the simulation and result section, where the outputs shown are satisfactory, and vindicates the real time applicability of the proposed technique, which will be useful for wide area protection.

6 Appendix

Table 9 The detailed parametric values of the network (Fig. 2)

Sl. No.	Element	Variables supporting the elements	Description
1	Utility		3-phase, 60 Hz, 154 kV
2	Distributed Generators	*DG 1, DG 2, DG 3* and *DG 4*	60 Hz, 575 V, 9 MW, DFIG based wind farms
3	Transformers	*Utility:* T_{r1}	22.9 kV/154 kV, 60 Hz, 47 MVA,
		Distribution: T_{r2}, T_{r3}, T_{r4} and T_{r5}	575 V/ 22.9 kV, 60 Hz, 10.5 MVA
4	Distributed Lines	DL_{AB} (20 km), DL_{AE} (16 km), DL_{BE} (12 km), DL_{BC} (02 km), DL_{CD} (04 km).	Pi section models, positive- and zero- sequence resistances (*r1*, *r0*)Ω/km = (0.07375, 0.4054) Ω/km, positive- and zero-sequence inductances (*l1*, *l0*)H/km = (0 3.4358×10^{-3}, 8.9524×10^{-3}) H/km, positive- and zero- sequence capacitances (*c1*, *c0*)F/km = (0.0075×10^{-6}, 0.0044×10^{-6}) F/km.
5	Loads	L_1 (constant PQ loads) L_2 (constant PQ loads) L_3 (constant PQ loads) L_4 (constant PQ loads) L_5 (constant PQ loads)	22.9 kV, 60 Hz, 12.0 MW, 0.50 MVAR 22.9 kV, 60 Hz, 10.5 MW, 0.25 MVAR 22.9 kV, 60 Hz, 11.0 MW, 0.45 MVAR 22.9 kV, 60 Hz, 12.0 MW, 0.15 MVAR 22.9 kV, 60 Hz, 10.5 MW, 0.05 MVAR
6	Battery Banks		1-MWh BESS is considered by integrating five 200-kWh LiFePO4 lithium–ion BESSs in parallel.

Authors' contributions
All authors read and approved the final manuscript.

Author details
[1]Electrical Engineering Department, Institute of Technical Education and Research, Institute of Technical Education and Research, Siksha O Anusandhan University, Bhubaneswar -751030, India. [2]Electrical and Electronics Engineering Department, GMR Institttute of Technology, Rajam, Andhra Pradesh -532127, India.

Received: 30 January 2017 Accepted: 16 July 2017
Published online: 14 August 2017

References

1. Arefifar, S. A., Yasser, A. R., & El-Fouly, T. H. (2013). Optimum microgrid design for enhancing reliability and supply-security. *IEEE Trans Smart Grid, 4*(3), 1567–1575.
2. Kroposki, B., Basso, T., DeBlasio, R. (2008). "Microgrid standards and technologies," IEEE Power and Energy Society General Meeting-Conversion and Delivery of Electrical Energy in the 21st Century, 1–4.
3. Khadkikar, V., Xu, D., & Cecati, C. (2017). Emerging power quality problems and state-of-the-art solutions. *IEEE Trans Ind Electron, 64*(1), 761–763.
4. Brearley, B. J., & Prabu, R. R. (2017). A review on issues and approaches for microgrid protection. *Renew Sust Energ Rev, 67*, 988–997.
5. Najy, W. K., Zeineldin, H. H., & Woon, W. L. (2013). Optimal protection coordination for microgrids with grid-connected and islanded capability. *IEEE Trans Ind Electron, 60*(4), 1668–1677.
6. Zeineldin, H. H., Sharaf, H. M., Ibrahim, D. K., & El-Zahab, E. E. (2015). Optimal protection coordination for meshed distribution systems with DG using dual setting directional over-current relays. *IEEE Trans Smart Grid, 6*(1), 115–123.
7. Etemadi, A. H., & Iravani, R. (2013). Overcurrent and overload protection of directly voltage-controlled distributed resources in a microgrid. *IEEE Trans Ind Electron, 60*(12), 5629–5638.
8. Dehghanpour, E., Karegar, H., Kheirollahi, R., Soleymani, T. (2016). "Optimal Coordination of Directional Overcurrent Relays in Microgrids by Using Cuckoo-Linear Optimization Algorithm and Fault Current Limiter,". *IEEE Trans Smart Grid*. doi: 10.1109/TSG.2016.2587725.
9. Nikolaidis, V. C., Papanikolaou, E., & Safigianni, A. S. (2016). A communication-assisted overcurrent protection scheme for radial distribution systems with distributed generation. *IEEE Trans Smart Grid, 7*(1), 114–123.
10. Zamani, M. A., Yazdani, A., & Sidhu, T. S. (Dec 2012). A communication-assisted protection strategy for inverter-based medium-voltage microgrids. *IEEE Trans Smart Grid, 3*(4), 2088–2099.
11. Mahat, P., Chen, Z., Bak-Jensen, B., & Bak, C. L. (Sep 2011). A simple adaptive overcurrent protection of distribution systems with distributed generation. *IEEE Trans Smart Grid, 2*(3), 428–437.
12. Khederzadeh, M. (2012). "Adaptive setting of protective relays in microgrids in grid-connected and autonomous operation," IET, 11th International Conference on Developments in Power Systems Protection (DPSP), 1–4..
13. Casagrande, E., Woon, W. L., Zeineldin, H. H., & Svetinovic, D. (2014). A differential sequence component protection scheme for microgrids with inverter-based distributed generators. *IEEE Trans Smart Grid, 5*(1), 29–37.
14. Zeineldin, H. H., El-Saadany, E. F., & Salama, M. M. (2006). Distributed generation micro-grid operation: Control and protection. *IEEE Power Syst Conf: Adv Metering, Protection, Control, Commun, Distributed Resour*, 105–111.
15. Ma, J., Wang, X., Zhang, Y., Yang, Q., & Phadke, A. G. (2012). A novel adaptive current protection scheme for distribution systems with distributed generation. *Int J Electr Power Energy Syst, 43*(1), 1460–1466.
16. Sortomme, E., Venkata, S. S., & Mitra, J. (2010). Microgrid protection using communication-assisted digital relays. *IEEE Transactions Power Deliv, 25*(4), 2789–2796.
17. Kar, S., & Samantaray, S. R. (2014). Time-frequency transform-based differential scheme for microgrid protection. *IET Generation, Transm Distrib, 8*(2), 310–320.
18. Krishnanand, K. R., & Dash, P. K. (2013). A new real-time fast S-transform for cross differential protection of shunt compensated power systems. *IEEE Trans Power Delivery, 28*(1), 402–410.
19. Dewadasa, M., Ghosh, A., Ledwich, G. (2011) "Protection of microgrids using differential relays," IEEE, 21st Australasian Universities Power Engineering Conference (AUPEC), 1–6.
20. Luna, A. C., Aldana, N. L., Graells, M., Vasquez, J. C., Guerrero, J. M. (2016). "Mixed-Integer-Linear-Programming based Energy Management System for Hybrid PV-wind-battery Microgrids: Modeling, Design and Experimental Verification," *IEEE Trans Power Electron, 32*(4):2769–2783.
21. Al Hassan, A Hashim, (2016). "Fault location identification of a hybrid HVDC-VSC system containing cable and overhead line segments using transient data," IEEE/PES Transmission and Distribution Conference and Exposition (T&D). pp. 1–5.
22. Patnaik, R. K., & Dash, P. K. (2015). Impact of wind farms on disturbance detection and classification in distributed generation using modified Adaline network and an adaptive neuro-fuzzy information system. *Appl Soft Comput, 30*, 549–566.
23. Patnaik, R. K., & Dash, P. K. (2016). Fast adaptive back-stepping terminal sliding mode power control for both the rotor-side as well as grid-side converter of the doubly fed induction generator-based wind farms. *IET Renewable Power Generation, 10*(5), 598–610.